Chapter 10
Effects of Domain Shapes and Mesh Discretization Error on the Morphological Evolution of Nonaqueous-Phase-Liquid Dissolution Fronts in Fluid-Saturated Porous Media

In the field of contaminant hydrology, both land contamination and land remediation problems are often encountered. Land contamination is known as the distribution of chemical and pollutants on land sites, while land remediation is known as the cleanup of chemical and pollutants on land sites that causes health concerns to the humans and the environment. When nonaqueous phase liquids (NAPLs), such as trichloroethylene, ethylene dibromide, benzene, toluene and so forth (Miller et al. 1990), are released to groundwater, they can reside in the form of disconnected ganglia or blobs as residual saturations within the pores of porous media. This process belongs to the land contamination problem. Some NAPLs (e.g. trichloroethylene and ethylene dibromide) are heavier than water, but others (e.g. benzene and toluene) are lighter than water. Although their solubilities in groundwater are very low, the effect of such NAPLs on the quality of groundwater resources is severe because of their relatively high toxicity. Thus, it is necessary to remove such NAPLs from the contaminated land site. This process belongs to the land remediation problem, which is the main focus of this chapter.

To develop effective and efficient methods for removing the residual NAPLs from contaminated land sites, the detailed transport mechanism of NAPLs in fluid-saturated porous media has been studied, both experimentally and analytically, during the past two decades (Miller et al. 1990, 1998; Geller and Hunt 1993; Powers et al. 1994; Imhoff et al. 1994, 1996, 2002, 2003a; Soerens et al. 1998; Willson et al. 1999; Seyedabbasi et al. 2008). Notable achievements from existing laboratory experiments are as follows: (1) mass transfer rates between a NAPL and an aqueous phase liquid can be determined in a quantitative manner; (2) the fingering phenomena of NAPL dissolution fronts have been observed at the laboratory (i.e. centimeter) scale; and (3) the linear stability theory has been employed to derive the critical condition that can be used to assess the instability of NAPL dissolution fronts in fluid-saturated porous media. For example, the Zhao number (Zhao et al. 2010c), which is a comprehensive dimensionless number, was proposed to represent the three major controlling mechanisms simultaneously

C. Zhao, *Physical and Chemical Dissolution Front Instability in Porous Media*, Lecture Notes in Earth System Sciences,
DOI: 10.1007/978-3-319-08461-9_10

taking place in a NAPL dissolution system. Based on the linear stability theory, a NAPL dissolution system may physically have three different kinds of states (Imhoff and Miller 1996; Zhao et al. 2008c, 2010b). In the supercritical state NAPL dissolution fingering occurs, but it does not occur in the subcritical state. The neutral condition (or state) is just the interface between the two. Correspondingly, three kinds of the Zhao numbers, namely the subcritical Zhao number, the critical Zhao number and the supercritical Zhao number, can be used to represent these three different kinds of states in the NAPL dissolution system. As a direct result of these achievements, both mathematical and computational models (Imhoff and Miller 1996; Miller et al. 1998; Zhao et al. 2010b) were developed to simulate the morphological evolution of NAPL dissolution fronts in fluid-saturated porous media. Nevertheless, the existing computational models are mainly limited to either a square domain or a rectangular domain, so that it is necessary to investigate the effects of different domain shapes on the morphological evolution of NAPL dissolution fronts in fluid-saturated porous media.

It needs to be pointed out that NAPL dissolution fingering requires regions of continuous NAPL saturation distribution (in the form of disconnected ganglia or blobs as residual within the pores of the porous medium) and has been observed in experiments with length scales of 7 cm and larger in the mean flow direction (Imhoff et al. 2003b). This requirement is unlikely to be satisfied for most two-dimensional experimental systems considered in the laboratory where a small amount of NAPL is spilled (Chen and Jawitz 2008; DiFilippo et al. 2010). However, as demonstrated previously (Parker and Park 2004; Christ et al. 2006, 2009; Gerhard et al. 2007), for large NAPL spill sites, continuous regions of residual NAPL occurred so that the above-mentioned requirement can be met. For example, in the work of Parker and Park (2004) a NAPL spillage event resulted in vertical fingers that on average were 30 cm in diameter. These fingers primarily contained residual NAPL. On the other hand, since most grid blocks used in current field-scale simulations were on the order of 30–50 cm (in the x and y dimensions), by necessity NAPL-contaminated grid blocks only represent continuous regions of NAPL (often residual) that exceed the 7 cm scale. As a result, these simulations might ignore NAPL dissolution fingering. It is a sub grid-block process that is not accounted for. The local (grid-block scale) rate of NAPL dissolution may not be important for many field problems, since the bypassing of water around NAPL-contaminated zones (Parker and Park 2004) is the slowest process limiting NAPL dissolution into surrounding groundwater. However, recent simulations indicate that for some systems local NAPL dissolution rates are important in heterogeneous media (Maji and Sudicky 2008). For such systems, NAPL dissolution fingering may be important. Thus, an understanding of NAPL dissolution fingering may be important for developing innovative remediation strategies and technologies to some NAPL contaminated groundwater systems.

In addition to NAPL dissolution fingering, preferential flow within NAPL contaminated zones can be also caused by either medium heterogeneity (Maji and Sudicky 2008) or variations in NAPL saturation, which in nature are not uniform in space (Grant and Gerhard 2007; Zhang et al. 2007). Medium heterogeneity

within NAPL-contaminated zones will result in a variation in aqueous-phase permeability. Some of this variation is associated with the variation in intrinsic permeability caused by the medium heterogeneity alone, while some is associated with the variation in NAPL saturation, which alters the relative permeability. Nevertheless, the mechanism of the preferential flow caused by NAPL dissolution fingering is different from that caused by medium heterogeneity. From the physical point of view, the former is considered as an emerging phenomenon due to the instability of a nonlinear system (Chadam et al. 1986, 1988; Ortoleva et al. 1987; Renard et al. 1998; Chen and Liu 2002, 2004; Chen et al. 2009; Zhao et al. 2008a, b, c, 2009, 2010a), while the latter is considered as the conventional phenomenon of a nonlinear system (Steefel and Lasaga 1990, 1994; Yeh and Tripathi 1991; Raffensperger and Garven 1995; Ormond and Ortoleva 2000; Alt-Epping and Smith 2001; Maji and Sudicky 2008).

Since the domain of a NAPL dissolution system in the real world may have many different shapes, it is difficult, if not impossible, to use a typical domain shape to represent all computational domains of NAPL dissolution systems encountered in the real world. However, for the purpose of investigating the effect of a domain shape on the interesting features associated with NAPL dissolution fingering, it is feasible to use a generic model of a specific shape (that is, to some extent, an artificial system) in the computational simulation, as long as some fundamental flow characteristics associated with irregular domains can be reasonably reflected in the generic model. On the other hand, due to the versatility and robustness of computational methods, any complicated domain shapes can be realistically simulated if their details can be precisely given. Compared with rectangular and square domains that are widely used in the previous studies (Imhoff and Miller 1996; Miller et al. 1998; Zhao et al. 2010b), some important flow characteristics associated with irregular domains are as follows (Zhang et al. 2007; Maji and Sudicky 2008). First, the pore-fluid flow in an irregular domain of a subcritical Zhao number is multi-directional (i.e. two-dimensional for a two-dimensional problem domain and three-dimensional for a three-dimensional problem domain) rather than unidirectional, just as what was observed in a rectangular or square domain of a subcritical Zhao. Second, the Darcy velocities of pore-fluid flow in an irregular domain of a subcritical Zhao number are not constant, but they are constant in a rectangular or square domain of a subcritical Zhao number. To select the domain shape of a generic model, a trapezoidal domain may be the reasonable choice from the following three points of view: (1) the above-mentioned flow characteristics such as the multi-directional flow and non-constant Darcy velocities can be simulated in a trapezoidal domain of a subcritical Zhao number; (2) due to the relatively simple shape, it is convenient to carry out a parameter study and theoretical estimation of mesh discretization error in the generic model of a trapezoidal domain; (3) the simulations are intended to investigate NAPL dissolution fingering in hypothetical systems to better understand the fingering process with converging and diverging flow. If complicated systems are used to represent the real world more realistically, there would be competing processes (e.g., NAPL dissolution fingering and flow bypass) that

would make it more difficult to understand NAPL dissolution fingering, which is the focus of this work. For these reasons, different trapezoidal computational domains are considered, in this chapter, to investigate the effects of domain shapes on the morphological evolution of NAPL dissolution fronts in two-dimensional fluid-saturated porous media.

To facilitate mathematical treatments in the process of deriving analytical solutions, it is commonly assumed that the pore-fluid flow within a two-dimensional fluid-saturated porous medium, which may be considered as an approximate representation of a horizontal cross-section (plane) in an aquifer, is parallel to the inflow at the entrance of the analytical domain, so that the second-order dispersion tensor can be considered as a function of the averaged linear velocity component in the inflow direction. This assumption may be valid for either a square domain or a rectangular domain where the inflow is parallel to two lateral boundaries of the domain. However, when the computational domain of a NAPL dissolution problem has a complicated shape, the pore-fluid flow in the computational domain is no longer parallel to the inflow, so that two components of the averaged linear velocity need to be considered in the second-order dispersion tensor. By using the general second-order dispersion tensor of two velocity components, it is also possible to validate the assumption that was used to derive analytical solutions for the NAPL dissolution problem in the fluid-saturated porous medium of a rectangular domain.

10.1 Governing Equations of NAPL Dissolution Problems in Two-Dimensional Fluid-Saturated Porous Media

From the previous studies (Imhoff and Miller 1996; Zhao et al. 2010c), a NAPL dissolution problem can be treated as a mass transport problem. As a result, the governing equations of the NAPL dissolution problem in a two-dimensional fluid-saturated porous medium can be expressed as follows:

$$\phi \frac{\partial S_n}{\partial t} = -\frac{K}{\rho_n}(C_{eq} - C), \tag{10.1}$$

$$\phi \frac{\partial}{\partial t} - [(1 - S_n)C] = \nabla \cdot [\phi(1 - S_n)\mathbf{D_h} \cdot \nabla C] + \nabla \cdot \left[\frac{k(S_n)}{\mu_a} C \nabla p_a\right] + K(C_{eq} - C), \tag{10.2}$$

$$\phi \frac{\partial S_n}{\partial t} = -\nabla \cdot \left[\frac{k(S_n)}{\mu_a} \nabla p_a\right] - \frac{K}{\rho_a}(C_{eq} - C), \tag{10.3}$$

where ϕ is the porosity; S_n is the NAPL saturation (i.e. the fraction of the void space occupied by the NAPL); ρ_a and ρ_n are the aqueous phase and nonaqueous phase densities; K is the mass transfer rate coefficient to express the exchange of the NAPL species from the nonaqueous phase to the aqueous phase; C is the solute

concentration of the NAPL species in the bulk aqueous phase and is equal to the ratio of the NAPL mass in the solution to the unit volume of the solution; C_{eq} is the equilibrium concentration of the NAPL species in the aqueous phase; $\mathbf{D_h}$ is the general dispersion tensor; $k(S_n)$ is the saturation-dependent permeability of the porous medium to aqueous phase flow; μ_a is the dynamic viscosity of the aqueous phase; and p_a is the aqueous phase pressure.

Note that although many NAPLs at contaminated sites are mixtures of compounds, only a single-species NAPL is considered in this chapter. This means that the equations used here describe a special class of NAPL spills. As a result, S_n, C and p_a are three independent variables in these three equations. As demonstrated previously (Imhoff and Miller 1996; Zhao et al. 2010c), Eq. (10.1) represents the mass conservation of the nonaqueous phase, while Eq. (10.3) represents the mass conservation of the aqueous phase. Since the nonaqueous phase is assumed to be immobile, an advective term does not appear in Eq. (10.1). However, since the aqueous phase is assumed to be mobile, an advective term must appear in Eq. (10.3). In addition, Eq. (10.2) represents the mass conservation of the NAPL species in the fluid-saturated porous medium.

Based on Darcy's law, the averaged linear velocity vector of the aqueous phase can be expressed as follows (Bear 1972):

$$\mathbf{v_a} = \begin{Bmatrix} v_{ax} \\ v_{ay} \end{Bmatrix} = \frac{-k(S_n)}{\phi(1 - S_n)\mu_a} \nabla p_a, \tag{10.4}$$

where $\mathbf{v_a}$ is the averaged linear velocity vector of the aqueous phase; v_{ax} and v_{ay} are the averaged linear velocity components in the x and y directions, respectively; other quantities have the same meanings as defined previously.

The following expressions are used for the saturation-dependent permeability (Imhoff and Miller 1996; Zhao et al. 2010c) and the dispersion tensor (Scheidegger 1961; Holzbecher 1998), respectively:

$$k(S_n) = k_f \left(\frac{1 - S_n - S_{ai}}{1 - S_{ai}} \right)^3, \tag{10.5}$$

$$\mathbf{D_h} = \begin{bmatrix} \tau D_m + \alpha_L \frac{v_{ax}^2}{v_a} + \alpha_T \frac{v_{ay}^2}{v_a} & (\alpha_L - \alpha_T) \frac{v_{ax} v_{ay}}{v_a} \\ (\alpha_L - \alpha_T) \frac{v_{ax} v_{ay}}{v_a} & \tau D_m + \alpha_L \frac{v_{ay}^2}{v_a} + \alpha_T \frac{v_{ax}^2}{v_a} \end{bmatrix}, \tag{10.6}$$

where k_f is the intrinsic permeability of the porous medium after the NAPL is completely dissolved; S_{ai} is the irreducible saturation of the aqueous phase; τ is the tortuosity of the porous medium; D_m is the molecular diffusivity of the NAPL species in the aqueous phase; α_T and α_L are the transversal and longitudinal dispersivities of the NAPL species in the aqueous phase; and v_a is the amplitude of the averaged linear velocity vector ($\mathbf{v_a}$) of the aqueous phase as follows:

$$v_a = \sqrt{v_{ax}^2 + v_{ay}^2}. \tag{10.7}$$

Note that the motivation of choosing a general form of the second-order dispersion tensor (expressed in Eq. (10.6)) is to consider the effect of two-dimensional pore-fluid flow on the dispersion in a trapezoidal domain.

The previous experimental results (Imhoff and Miller 1996) indicate that the mass transfer rate coefficient (K) can be expressed in the following form:

$$K = \beta_0 S_n^{\beta_1}, \tag{10.8}$$

where β_0 is a function of the porous medium, the NAPL, and the velocity, viscosity and density of the aqueous phase fluid; β_1 is a constant.

If the computational domain of a NAPL dissolution system has a trapezoidal shape (as shown in Fig. 10.1), which may be considered either as the experimental specimen used in a laboratory experiment or as the approximate representation of a pie slice in a horizontal cross-section (plane) for radial flow in an aquifer, then the boundary conditions of the problem can be expressed as follows:

$$C = 0, \quad S_n = 0, \quad \frac{\partial p_a}{\partial x} = p'_{axf0} \quad (x = 0), \tag{10.9}$$

$$p_a = p_{a0} \quad (x = L_x), \tag{10.10}$$

$$\frac{\partial C}{\partial n} = 0, \quad \frac{\partial p_a}{\partial n} = 0 \quad (\text{at two lateral boundaries}), \tag{10.11}$$

where S_{n0} is the initial saturation of the NAPL; p'_{axf0} is the pressure gradient of the aqueous phase on the upstream boundary; p_{a0} is the pressure of the aqueous phase on the downstream boundary; L_x is the length of the problem domain in the x direction; and n is the normal vector of the lateral boundary. Since p'_{axf} drives the aqueous phase fluid flow continuously along the positive x direction, it has a negative algebraic value (i.e. $p'_{axf} < 0$) for the problem under consideration.

Except for the upstream boundary, the initial conditions of the problem for the rest of the computational domain are as follows:

$$C = C_{eq}, \quad S_n = S_{n0} \quad (0 < x \leq L_x). \tag{10.12}$$

Since the use of dimensionless governing equations has some advantages in dealing with problems of multi-scales and multi-processes (Zhao et al. 2009), it is useful to transform the above-mentioned governing equations of the problem into the following dimensionless form:

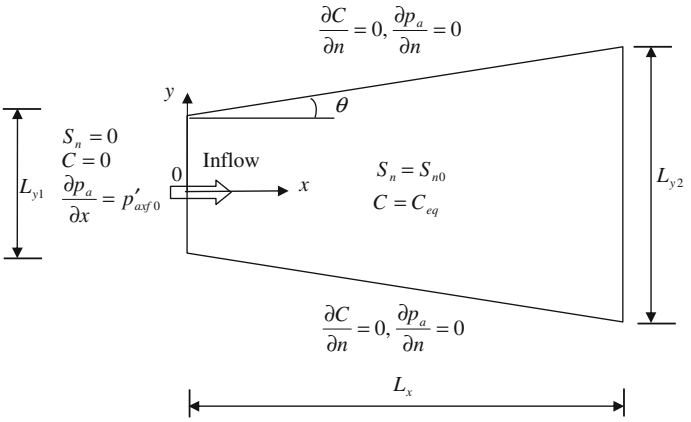

Fig. 10.1 Geometry and boundary conditions for the NAPL dissolution problem on the basis of dimensional quantities

$$\frac{\partial S_n}{\partial \bar{t}} + S_n^{\beta_1}(1-\bar{C}) = 0, \tag{10.13}$$

$$\varepsilon \frac{\partial}{\partial \bar{t}}[(1-S_n)\bar{C}] - \nabla \cdot \{[(1-S_n)\bar{\mathbf{D}}_\mathbf{h}] \cdot \nabla \bar{C} + \bar{C}\bar{\psi}(S_n)\nabla \bar{p}_a\} + \frac{\partial S_n}{\partial \bar{t}} = 0, \tag{10.14}$$

$$\varepsilon \frac{\partial S_n}{\partial \bar{t}} + \nabla \cdot [\bar{\psi}(S_n)\nabla \bar{p}_a] + \frac{\varepsilon}{\bar{\rho}_a} S_n^{\beta_1}(1-\bar{C}) = 0, \tag{10.15}$$

where

$$\bar{\mathbf{D}}_\mathbf{h} = \begin{bmatrix} \bar{d}_{11} & \bar{d}_{12} \\ \bar{d}_{21} & \bar{d}_{22} \end{bmatrix}, \tag{10.16}$$

where

$$\bar{d}_{11} = 1 + \frac{\bar{\psi}(S_n)}{1-S_n} \frac{\bar{\alpha}_L \left(\frac{\partial \bar{p}_a}{\partial \bar{x}}\right)^2 + \bar{\alpha}_T \left(\frac{\partial \bar{p}_a}{\partial \bar{y}}\right)^2}{\sqrt{\left(\frac{\partial \bar{p}_a}{\partial \bar{x}}\right)^2 + \left(\frac{\partial \bar{p}_a}{\partial \bar{y}}\right)^2}}, \quad \bar{d}_{22} = 1 + \frac{\bar{\psi}(S_n)}{1-S_n} \frac{\bar{\alpha}_L \left(\frac{\partial \bar{p}_a}{\partial \bar{y}}\right)^2 + \bar{\alpha}_T \left(\frac{\partial \bar{p}_a}{\partial \bar{x}}\right)^2}{\sqrt{\left(\frac{\partial \bar{p}_a}{\partial \bar{x}}\right)^2 + \left(\frac{\partial \bar{p}_a}{\partial \bar{y}}\right)^2}},$$

$$\bar{d}_{21} = \bar{d}_{21} = \frac{\bar{\psi}(S_n)}{1-S_n} \frac{(\bar{\alpha}_L - \bar{\alpha}_T)\frac{\partial \bar{p}_a}{\partial \bar{x}} \frac{\partial \bar{p}_a}{\partial \bar{y}}}{\sqrt{\left(\frac{\partial \bar{p}_a}{\partial \bar{x}}\right)^2 + \left(\frac{\partial \bar{p}_a}{\partial \bar{y}}\right)^2}}.$$

Note that the following dimensionless quantities are used for deriving the above dimensionless governing equations of the problem:

$$\bar{x} = \frac{x}{L^*}, \quad \bar{y} = \frac{y}{L^*}, \quad \bar{L}_x = \frac{L_x}{L^*}, \quad \bar{L}_{y1} = \frac{L_{y1}}{L^*}, \quad \bar{L}_{y2} = \frac{L_{y2}}{L^*}, \quad \bar{C} = \frac{C}{C_{eq}}, \quad (10.17)$$

$$\bar{p}_a = \frac{p_a}{p_a^*}, \quad \bar{\alpha}_L = \frac{\alpha_L}{L^*}, \quad \bar{\alpha}_T = \frac{\alpha_T}{L^*}, \quad \bar{n} = \frac{n}{L^*}, \quad \bar{t} = \frac{t}{t^*}\varepsilon, \quad \varepsilon = \frac{C_{eq}}{\rho_n} \ll 1, \quad (10.18)$$

where

$$t^* = \frac{\phi}{\beta_0}, \quad L^* = \sqrt{\tau D_m t^*}, \quad p_a^* = \frac{\phi \tau D_m}{\psi(S_{nf})}, \quad (10.19)$$

$$\bar{\mathbf{D}}_\mathbf{h} = \frac{\mathbf{D}_\mathbf{h}}{\tau D_m}, \quad \bar{\psi}(S_n) = \frac{\psi(S_n)}{\psi(S_{nf})}, \quad \psi(S_n) = \frac{k(S_n)}{\mu_a}, \quad (10.20)$$

where $\psi(S_{nf})$ is the value of $\psi(S_n)$ at $S_n = 0$. Physically, the dimensionless time (i.e. $\bar{t}$) represents some scaling between the real time and intrinsic time (i.e. t^*) of the NAPL dissolution system (Zhao et al. 2010c).

It needs to be pointed out that a small dimensionless quantity (i.e. ε) is defined in Eq. (10.18), for representing the dissolution ratio of the NAPL equilibrium concentration to the mass density of the NAPL. Since this small dimensionless quantity, known as the NAPL dissolution ratio, can be used not only to mathematically determine the instability conditions of NAPL dissolution fronts in supercritical dissolution systems, but also to computationally simplify the numerical algorithm in the related computational simulation (Zhao et al. 2010a), it is kept as a parameter for the normalization of time.

Although the NAPL dissolution ratio (i.e. ε) is equal to C_e/ρ_n and ρ_n is a constant, it is the NAPL dissolution ratio (i.e. ε), rather than the equilibrium concentration (i.e. C_e) alone, that can have a significant effect on both the propagation velocity and the morphological shape of a NAPL dissolution front. To explain this point, it is necessary to briefly review the propagation mechanism of a NAPL dissolution front in the fluid-saturated porous medium as follows. In a NAPL dissolution system, the residual NAPL is resided in the form of disconnected ganglia or blobs within the pores of the porous medium. The amount of the residual NAPL per unit pore volume of the porous medium is equal to the product of the residual saturation (i.e. S_n) and the density of the residual NAPL. To remove the residual NAPL from the porous medium, the fluid (e.g. water) is injected, with a given velocity, into the region where the residual NAPL resides. Since the equilibrium concentration (i.e. C_e) represents the maximum limit that the residual NAPL can be dissolved in the fluid, the residual NAPL amount carried by the flowing fluid when it passes the NAPL dissolution front is therefore limited. After the previous flowing fluid passes the NAPL dissolution front, the fresh flowing fluid reaches the NAPL dissolution front so that some of the undissolved residual NAPL at the NAPL dissolution front can be dissolved into the fresh flowing fluid and carried away from the NAPL dissolution front by the fresh flowing fluid. Such

processes continue until all the residual NAPL at the NAPL dissolution front is completely dissolved and carried away by the flowing fluid. At this stage, the NAPL dissolution front will propagate forwards. This means that in a NAPL dissolution system, there are two velocities (or speeds): one is the flowing fluid velocity, another is the propagation velocity of the NAPL dissolution front. Generally, the propagation velocity of a NAPL dissolution front is slower than that of the flowing fluid. According to the above analysis, it is recognized that the propagation velocity of a NAPL dissolution front depends directly on the NAPL dissolution ratio (i.e. ε), which can be used to determine how much flowing fluid should pass the NAPL dissolution front to enable it to propagate, rather than the equilibrium concentration (i.e. C_e) alone.

The boundary conditions can be also expressed in the following dimensionless form:

$$\bar{C} = 0, \quad S_n = 0, \quad \frac{\partial \bar{p}_a}{\partial \bar{x}} = \bar{p}'_{axf0} \quad (\bar{x} = 0), \tag{10.21}$$

$$\bar{p}_a = \bar{p}_{a0} \quad (\bar{x} = \bar{L}_x), \tag{10.22}$$

$$\frac{\partial \bar{C}}{\partial \bar{n}} = 0, \quad \frac{\partial \bar{p}_a}{\partial \bar{n}} = 0 \quad (\text{at two lateral boundaries}), \tag{10.23}$$

where $\bar{p}'_{axf0}$ is the dimensionless pressure gradient of the aqueous phase on the upstream boundary; $\bar{p}_{a0}$ is the dimensionless pressure of the aqueous phase on the downstream boundary.

Similarly, the initial conditions of the problem can be rewritten in a dimensionless form as follows:

$$\bar{C} = 1, \quad S_n = S_{n0} \quad (0 < \bar{x} \leq \bar{L}_x). \tag{10.24}$$

Note that Eq. (10.24) assumes a uniform distribution field of residual NAPL saturation, which may be achieved either in the experimental specimen (of trapezoidal shape) on the laboratory scale or in large NAPL spill sites where the migration of the spilled NAPL has ceased in the system (Imhoff et al. 2003b; Gerhard et al. 2007).

To solve the dimensionless governing equations of a NAPL dissolution problem in a two-dimensional fluid-saturated porous medium, a numerical procedure consisting of a combination of the finite difference and finite element methods (Zienkiewicz 1977; Zhao et al. 2009) has been proposed in a previous study (Zhao et al. 2010a). In the proposed numerical procedure, the finite difference method is used to discretize time, while the finite element method is used to discretize space. To ensure the correctness and accuracy of the resulting numerical simulations, the proposed numerical procedure has been verified by some benchmark problems for which analytical solutions are available for comparison. Since the dimensionless governing equations of a NAPL dissolution system are highly nonlinear, the

segregated algorithm, in which Eqs. (10.13)–(10.15) are solved separately and iteratively in a sequential manner, was used to derive the formulation of the proposed numerical procedure (Zhao et al. 2011). For the sake of completeness of this chapter, only the final discretized equations of the NAPL dissolution system are given below. If readers are interested in the detailed derivation processes of these equations, please refer to Chap. 9 or a previous publication (Zhao et al. 2011).

By following the numerical procedure used in Chap. 9 or a previous study (Zhao et al. 2011), the dimensionless governing equations (i.e. Eqs. (10.13)–(10.15)) of a NAPL dissolution system under the condition of $\varepsilon \ll 1$ can be expressed as follows:

$$\left[\frac{1}{\Delta\bar{t}}(S_n)_{\bar{t}}^{1-\beta_1} + \beta_1(1-\bar{C}_{\bar{t}+\Delta\bar{t}})\right](\Delta S_n)_{\bar{t}+\Delta\bar{t}} = -(S_n)_{\bar{t}}(1-\bar{C}_{\bar{t}+\Delta\bar{t}}), \tag{10.25}$$

$$\begin{aligned}\left\{\frac{\varepsilon}{\Delta\bar{t}}[1-(S_n)_{\bar{t}+\Delta\bar{t}}] + (S_n)_{\bar{t}+\Delta\bar{t}}^{\beta_1}\right\}\bar{C}_{\bar{t}+\Delta\bar{t}} - \nabla\cdot[(1-(S_n)_{\bar{t}+\Delta\bar{t}})(\bar{\mathbf{D}}_{\mathbf{h}})_{\bar{t}+\Delta\bar{t}}]\cdot\nabla\bar{C}_{\bar{t}+\Delta\bar{t}} \\ - \nabla(\bar{p}_a)_{\bar{t}+\Delta\bar{t}}\cdot[\bar{\psi}((S_n)_{\bar{t}+\Delta\bar{t}})\nabla\bar{C}_{\bar{t}+\Delta\bar{t}}] = \frac{\varepsilon}{\Delta\bar{t}}[1-(S_n)_{\bar{t}+\Delta\bar{t}}]\bar{C}_{\bar{t}} + (S_n)_{\bar{t}+\Delta\bar{t}}^{\beta_1},\end{aligned} \tag{10.26}$$

$$\nabla\cdot\left[\bar{\psi}((S_n)_{\bar{t}+\Delta\bar{t}})\nabla(\bar{p}_a)_{\bar{t}+\Delta\bar{t}}\right] = \varepsilon\left(1-\frac{1}{\bar{\rho}_a}\right)(S_n)_{\bar{t}+\Delta\bar{t}}^{\beta_1}(1-\bar{C}_{\bar{t}+\Delta\bar{t}}), \tag{10.27}$$

where $(S_n)_{\bar{t}}$ and $(S_n)_{\bar{t}+\Delta\bar{t}}$ are the saturations of the NAPL at the previous and current time-steps; $(\Delta S_n)_{\bar{t}+\Delta\bar{t}}$ is the saturation increment of the NAPL at the current time-step; $\bar{C}_{\bar{t}}$ and $\bar{C}_{\bar{t}+\Delta\bar{t}}$ are the dimensionless concentrations of the NAPL at the previous and current time-steps respectively; $(\bar{p}_a)_{\bar{t}+\Delta\bar{t}}$ is the dimensionless pressure of the aqueous phase at the current time-step; $\Delta\bar{t}$ is the dimensionless time increment at the current time-step.

It should be pointed out that the main advantages in using dimensionless variables and governing equations are as follows (Zhao et al. 2008c): (1) solutions for dimensionless variables describe the behaviour of a family of problems rather than that of a particular problem. This makes the solutions more generally applicable. (2) Dimensionless variables can be used to measure the relative importance of various terms in governing equations, so that the dominant physical phenomenon can be identified for the problem. This provides a clear focus for the effective and efficient modelling of the problem. (3) Dimensionless equations can result in a significant reduction in the large differences between orders of magnitude for some terms in the corresponding dimensional equations, just like the partial differential equations that are used to describe the NAPL dissolution instability problem in this chapter. This generally makes the numerical solution more accurate and stable. For these reasons, dimensionless variables and governing equations are used in the following computational simulations. Nevertheless, the obtained dimensionless solutions can be easily transferred, if necessary, into dimensional solutions, as demonstrated in a previous study (Zhao et al. 2008c). As a result, the parametric study of a NAPL dissolution system can be

directly carried out through the related dimensionless solutions. For instance, from the Zhao number (Zhao et al. 2010c), we can immediately know that an increase in the Darcy velocity of the dissolved region (i.e. V_{axf}) will cause an increase in the Zhao number of the NAPL dissolution system, so that the NAPL dissolution system becomes more unstable. On the other hand, an increase in the NAPL dissolution rate (i.e. β_0) will cause a decrease in the Zhao number of the NAPL dissolution system, so that the NAPL dissolution system becomes more stable.

10.2 Effects of Domain Shapes on the Morphological Evolution of NAPL Dissolution Fronts in Supercritical Systems

As mentioned previously, trapezoidal domains can be used to appropriately represent some fundamental flow characteristics that occur in irregular domains. For this reason, different trapezoidal computational domains are considered to investigate the effects of domain shapes on the morphological evolution of NAPL dissolution fronts in two-dimensional fluid-saturated porous media of supercritical Zhao numbers (Zhao et al. 2010c). Figure 10.1 shows the geometrical and boundary conditions for the NAPL dissolution problem of a typical trapezoidal domain, which is geometrically symmetrical to the x axis. Since the geometrical shape of such a trapezoidal computational domain can be represented by the divergent angle (i.e. θ) between a horizontal line and a lateral boundary, this angle is defined as a geometrical parameter in the corresponding computations. Note that if θ is equal to zero, then the trapezoidal shape degenerates to a rectangular one.

Based on the previous experimental measurement results that were calibrated by several laboratory tests (Imhoff and Miller 1996; Imhoff et al. 1996; Miller et al. 1998), the following parameters are selectively used in the corresponding computational models: the initial saturation (S_{n0}) of the NAPL (i.e. trichloroethylene (TCE)) is 0.2; the irreducible saturation (S_{ai}) of the aqueous phase fluid is 0.15; the dimensionless longitudinal and transverse dispersivities ($\bar{\alpha}_L$ and $\bar{\alpha}_T$) are 0.2 and 0.02, respectively; the ratio (ε) of the equilibrium concentration of the NAPL species in the aqueous phase fluid to the density of the NAPL itself is 0.001; the density ratio ($\bar{\rho}_a$) of the aqueous phase fluid to the NAPL is 1.0/1.46; the value of β_1 is 0.87. Since the dimensionless governing equations (i.e. Eqs. (10.13)–(10.15)) are used in the numerical simulation, we do not need to use specific values of the quantities such as β_0, medium porosity and tortuosity, molecular diffusivity of the NAPL and the Darcy flux at the inlet in this investigation. These quantities are represented by a comprehensive dimensionless number, known as the Zhao number (Zhao et al. 2012), in the corresponding numerical simulation.

To simulate the propagation of NAPL dissolution fronts appropriately, the finite element size has been varied to ensure that the numerical dispersion does not affect the numerical simulation results in a rectangular domain, for which analytical solutions are available for comparison with the numerical solution. Through the

mesh size sensitivity analysis, it is confirmed that as long as the finite element size satisfies the mesh Peclet criterion (Daus et al. 1985), the numerical dispersion can be minimized in the computational simulation. As a result, the whole computational domain is simulated by 120,000 four-node quadrilateral elements of 120,701 nodal points in total. For the purpose of investigating the instability of a NAPL dissolution system, it is common practice to perturb the homogeneous distribution field of the initial NAPL saturation (S_{n0}) with a small amount (Zhao et al. 2010c). If the NAPL dissolution system is in a stable state, then such a small perturbation does not affect the propagation behaviour of the NAPL dissolution front in the homogeneous distribution field of the initial NAPL saturation (S_{n0}), so that an initial planar NAPL dissolution-front remains the planar shape. However, If the NAPL dissolution system is in an unstable state, then such a small perturbation can significantly affect the propagation behaviour of the NAPL dissolution front in the homogeneous distribution field of the initial NAPL saturation (S_{n0}), so that an initial planar NAPL dissolution-front can evolve into different irregular shapes. For this reason, the initial residual saturation field of the NAPL is randomly perturbed by a small amount of 1 % of the originally-input saturation of the NAPL (i.e. $S_{n0} = 0.2$) before running the computational model. This means that the resulting initial residual saturation is of a random distribution, which has a mean value of the homogeneous residual saturation (i.e. $S_{n0} = 0.2$) and a variation of 0.002 (i.e. 1 % of $S_{n0} = 0.2$) in the whole computational domain. Thus, the initial homogeneous distribution field of the NAPL saturation (S_{n0}) is replaced and reassigned by a slightly perturbed non-homogeneous distribution field of the NAPL saturation before running the computational model. Using the characteristic length (i.e. L^*) as the length scaling factor, the dimensionless length (i.e. $\bar{L}_x = L_x/L^*$) of the computational domain is 6284 in the $\bar{x}$ direction, while the dimensionless length (i.e. $\bar{L}_{y1} = L_{y1}/L^*$) of the left boundary is fixed to 3142, 2734, 2329 and 2046 in the $\bar{y}$ direction, respectively, when four different computational domains, namely $\theta = 0°$, 4°,11° and 20°, are used to investigate the effects of domain shapes on the morphological evolution of NAPL dissolution fronts in supercritical systems. The Zhao number used for all the four computational models (at the entrance of the flow) is 1.0, while the dimensionless time-step length is 3.2. From the previous theoretical study (Zhao et al. 2010c), the critical Zhao number is 3.34×10^{-3} in the case of $\theta = 0°$. As the Zhao number is much greater than its critical value, it is expected that the NAPL dissolution system under consideration is in a supercritical state. Although different values of the Zhao number can have significant effects on the morphological evolution of NAPL dissolution fronts, this issue is not considered here because it has been addressed in a rectangular domain (Zhao et al. 2011) and the main focus of this chapter is to investigate the effect of domain shapes on the morphological evolution of NAPL dissolution fronts in the fluid-saturated porous medium.

Figures 10.2, 10.3, 10.4 and 10.5 show the effects of domain shapes on the morphological evolution of NAPL dissolution fronts in the fluid-saturated porous medium at four different time instants, namely $\bar{t} = 160$, 640, 1120 and 1600,

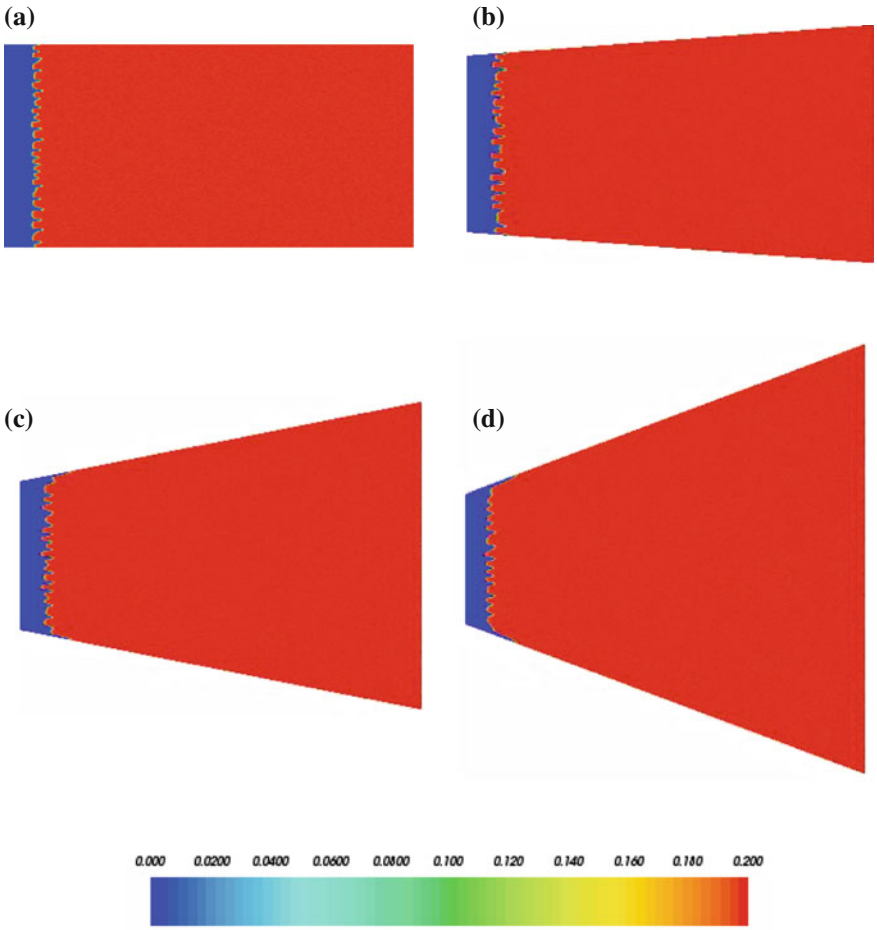

Fig. 10.2 Effects of domain shapes on the evolution of NAPL dissolution fronts represented by residual saturation in the fluid-saturated porous medium ($\bar{t} = 160$): **a** $\theta = 0$; **b** $\theta = 4^\circ$; **c** $\theta = 11^\circ$; **d** $\theta = 20^\circ$

respectively. In these figures, the residual saturation of a NAPL is used to represent the NAPL dissolution front. It is observed that domain shapes can significantly affect not only the propagating speed of a NAPL dissolution front, but the morphological evolution pattern of the NAPL dissolution front as well. At the early stage of the computational simulation, the NAPL dissolution front evolves from the injected planar shape at the left boundary of the computational model into an irregular shape. For a planar NAPL dissolution-front propagating in an infinite domain, the previous theoretical analysis demonstrated that the propagating speed of the planar NAPL dissolution-front is directly proportional to the Darcy velocity of the aqueous phase fluid within the fluid-saturated porous medium. In the case of a trapezoidal domain, an increase in the divergent angle (i.e. θ) of the trapezoidal

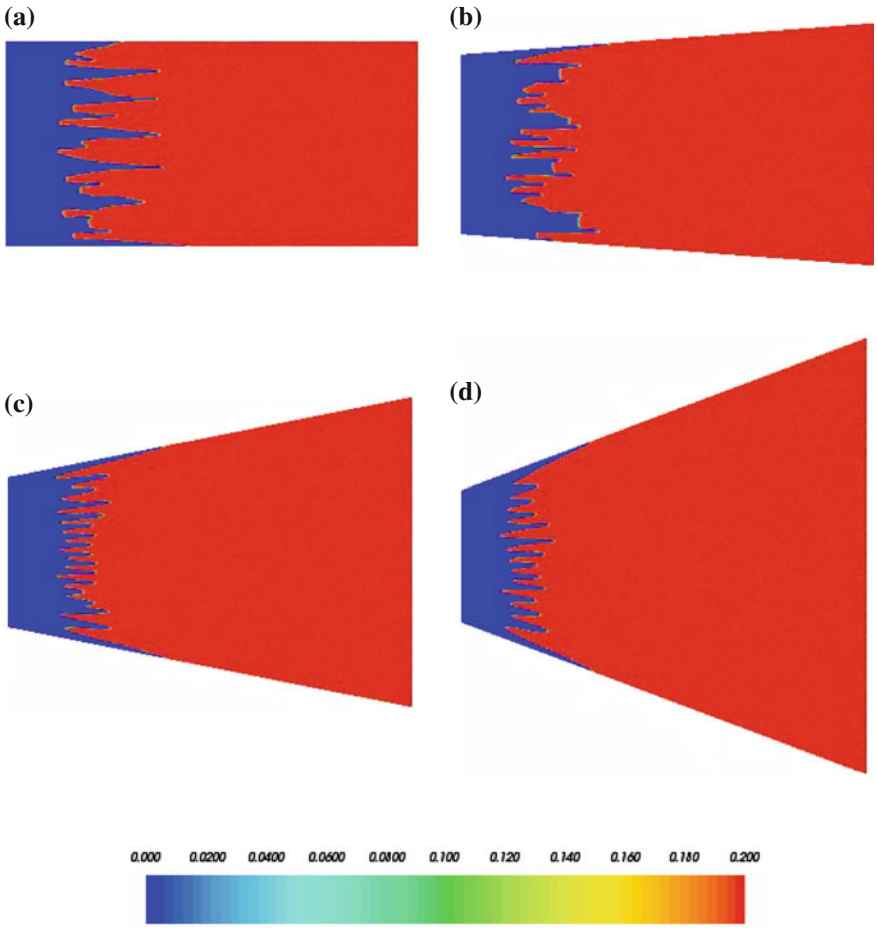

Fig. 10.3 Effects of domain shapes on the evolution of NAPL dissolution fronts represented by residual saturation in the fluid-saturated porous medium ($\bar{t} = 640$): **a** $\theta = 0$; **b** $\theta = 4°$; **c** $\theta = 11°$; **d** $\theta = 20°$

domain can lead to an increase in the area (or the length in the two-dimensional case) of a vertical cross-section that is perpendicular to the inflow direction of the aqueous phase fluid within the trapezoidal domain. From the mass conservation point of view, such an increase in the divergent angle of the trapezoidal domain can cause a decrease in the Darcy velocity of the aqueous phase fluid on the area of the vertical cross-section within the trapezoidal domain. Thus, with an increase in the divergent angle of a trapezoidal domain, the propagating speed of a planar NAPL dissolution-front decreases accordingly within the fluid-saturated porous medium. Since this theoretical prediction has good agreement with the numerical results (as shown in Fig. 10.2) at the early stage of the computational simulation, it has demonstrated that the computational model used in this investigation can

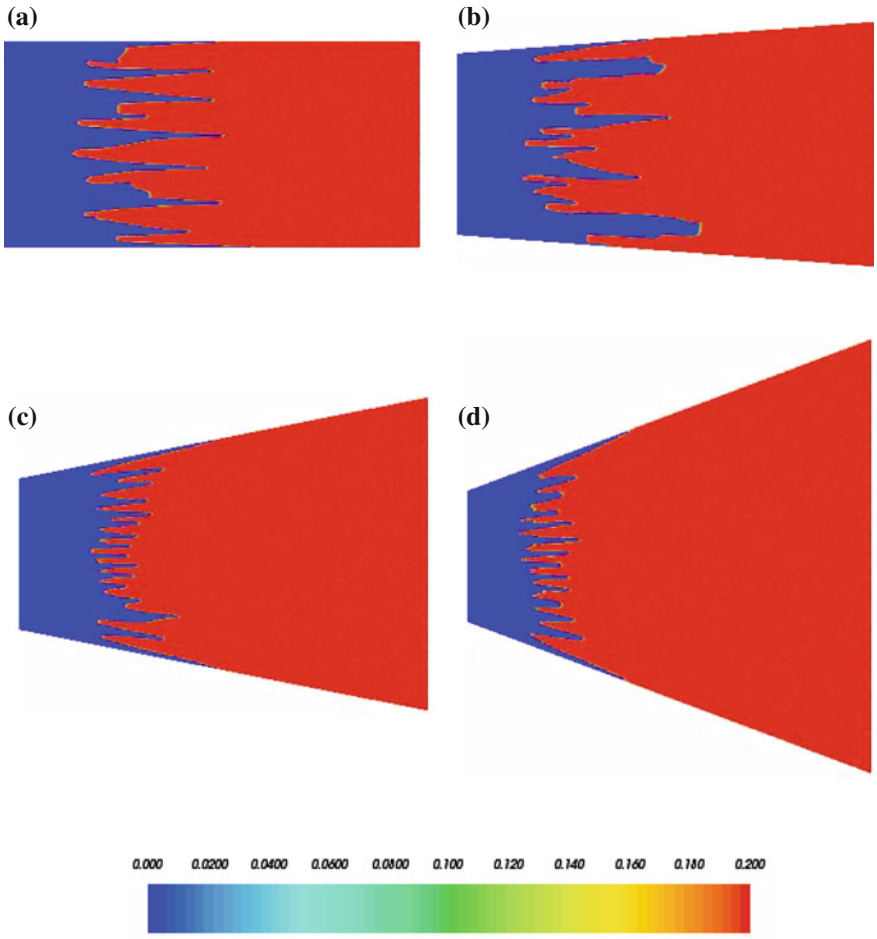

Fig. 10.4 Effects of domain shapes on the evolution of NAPL dissolution fronts represented by residual saturation in the fluid-saturated porous medium ($\bar{t} = 1120$): **a** $\theta = 0$; **b** $\theta = 4°$; **c** $\theta = 11°$; **d** $\theta = 20°$

produce reliable numerical results for simulating the evolution of a planar NAPL dissolution-front in the fluid-saturated porous medium of a trapezoidal shape.

However, it is very difficult, if not impossible, to predict theoretically the propagating speed of an irregular NAPL dissolution-front within the fluid-saturated porous medium of supercritical Zhao numbers. In this situation, the average Darcy velocity on the area of a vertical cross-section can be used to investigate the effect of domain shapes on the average propagating speed of the irregular NAPL dissolution-front. Since the aqueous phase fluid should be conservative on a vertical cross-section perpendicular to the inflow direction of the aqueous phase fluid within the trapezoidal domain, the average Darcy velocity on this vertical cross-section can be expressed in the weighted form as follows:

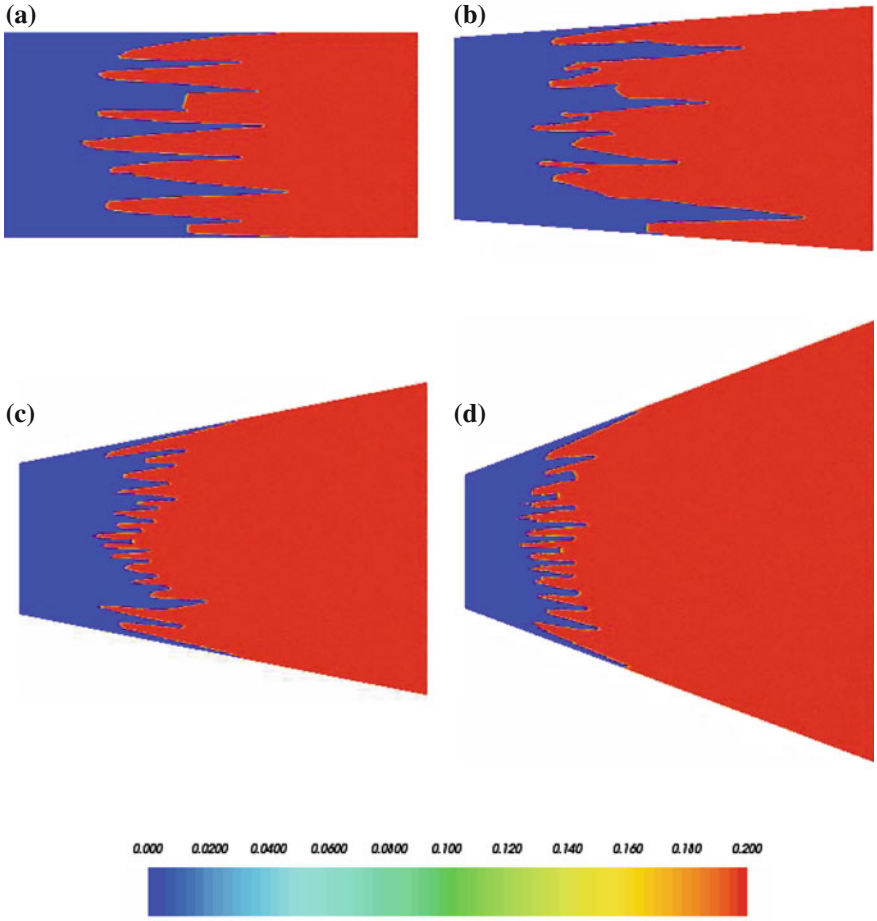

Fig. 10.5 Effects of domain shapes on the evolution of NAPL dissolution fronts represented by residual saturation in the fluid-saturated porous medium ($\bar{t} = 1600$): **a** $\theta = 0$; **b** $\theta = 4°$; **c** $\theta = 11°$; **d** $\theta = 20°$

$$\bar{v}_{Darcy} = \frac{\int_{-\frac{L_y}{2}}^{+\frac{L_y}{2}} v_{Darcy} dy}{L_y}, \tag{10.28}$$

where L_y is the length of the vertical cross-section; v_{Darcy} is the Darcy velocity at a point of the vertical cross-section; $\bar{v}_{Darcy}$ is the average Darcy velocity on the vertical cross-section.

Based on the average Darcy velocity concept, it is possible to examine how the domain shape of a computational model affects the average propagating speed of an irregular NAPL dissolution-front within the fluid-saturated porous medium. For

the given location of a vertical cross-section in a trapezoidal domain, an increase in the divergent angle of the trapezoidal domain leads to an increase in the length of the vertical cross-section parallel to the y direction, so that there is a decrease in the average Darcy velocity on this vertical cross-section in the trapezoidal domain. Generally, the average propagating speed of an irregular NAPL dissolution-front decreases gradually as a result of an increase in the divergent angle of the trapezoidal domain. This phenomenon can be observed from the numerical simulation results shown in Figs. 10.3, 10.4 and 10.5. However, in the case of $\theta = 4°$, the strong mergence of several irregular fingering fronts takes place within the computational domain. Due to this mergence, the fluid flow in the merged fingers of wider flow channels becomes much stronger than that in the unmerged small fingers, so that the tip of the dissolution front represented by the strongly merged finger in the case of $\theta = 4°$ has propagated faster than that represented by the weakly merged finger in the rectangular case.

In terms of the morphological evolution pattern of an irregular NAPL dissolution-front, the domain shape of a computational model can affect the total numbers of irregular fingers in the fluid-saturated porous medium of supercritical Zhao numbers. For a given position at the x axis, the trapezoidal domain of a large divergent angle (i.e. θ) can provide more space in the vertical direction, compared with the trapezoidal domain of a small divergent angle. As a result, the total number of irregular fingers obtained from the trapezoidal domain of a large divergent angle is usually greater than that obtained from the trapezoidal domain of a small divergent angle. For example, in the case of $\bar{t} = 1600$, the total number of irregular fingers in the rectangular domain is equal to 8, while it is equal to 14 in the trapezoidal domain with a divergent angle of 20°. Nevertheless, as shown in Figs. 10.3, 10.4 and 10.5, the irregular fingers in the trapezoidal domain of a small divergent angle can grow much wider than those in the trapezoidal domain of a large divergent angle.

Figure 10.6 shows the effects of domain shapes on the distributions of the NAPL dimensionless concentration in the fluid-saturated porous medium at $\bar{t} = 1600$. Since the small perturbation grows with time for a supercritical NAPL dissolution system, the initial planar front of the NAPL dimensionless concentration evolves gradually into an irregular fingering one. With an increase in the dimensionless time, the amplitude of the irregular fingering NAPL concentration front increases significantly, indicating that the NAPL concentration front is morphologically unstable during its propagation within the computational domain. Compared with the computational simulation results shown in Fig. 10.5, both the NAPL residual saturation and the NAPL dimensionless concentration have similar propagation fronts because the dimensionless concentration of the NAPL approaches zero when the NAPL is completely dissolved in the upstream direction of the NAPL dissolution front. Once the NAPL is completely dissolved, the NAPL residual saturation also becomes zero in the upstream direction of the NAPL dissolution front.

It is interesting to examine NAPL dissolution fingering in a convergent trapezoidal domain where the divergent angle (as defined in Fig. 10.1) has a negative

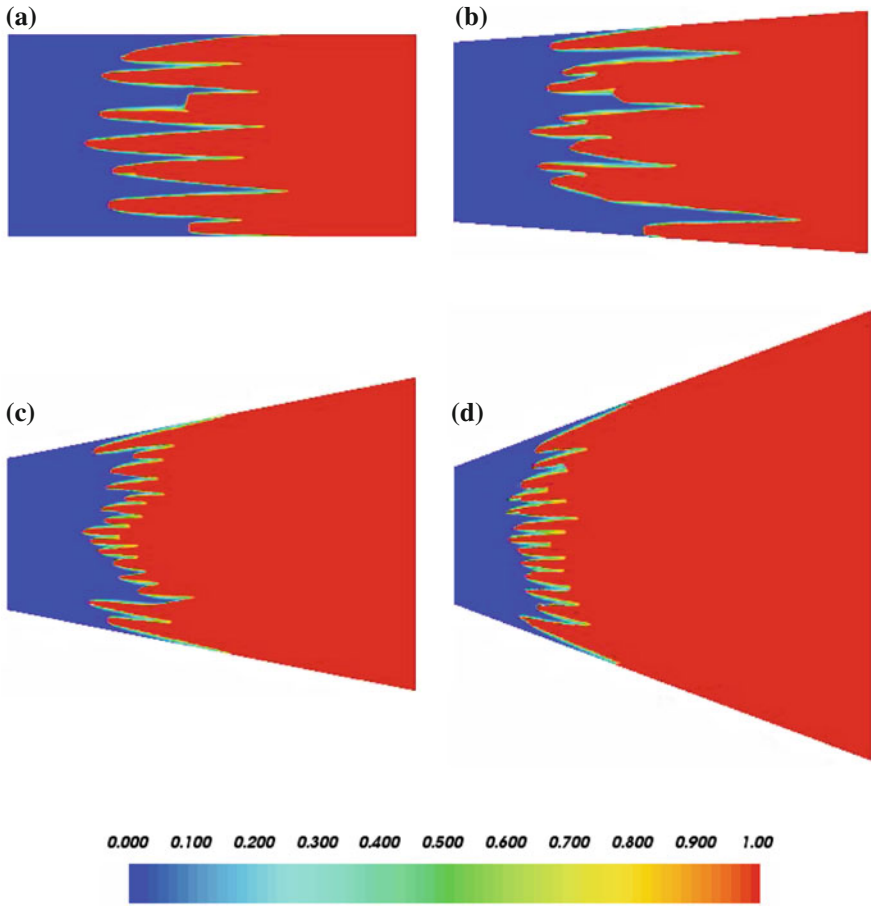

Fig. 10.6 Effects of domain shapes on the distributions of the NAPL dimensionless concentration in the fluid-saturated porous medium ($\bar{t} = 1600$): **a** $\theta = 0$; **b** $\theta = 4°$; **c** $\theta = 11°$; **d** $\theta = 20°$

value for θ. Since convergent trapezoidal domains can result in Darcy velocities increasing with an increase in the distance from the entrance of the injected flow, they may produce some interesting effects on NAPL dissolution fingering. For this purpose, a negative value of θ (i.e. $\theta = -20°$) is used to run the corresponding computational simulation of NAPL dissolution fingering in a convergent trapezoidal domain. Figure 10.7 shows the effects of the convergent domain shape (in the case of $\theta = -20°$) on the evolution of NAPL dissolution fronts (represented by residual saturation) in the fluid-saturated porous medium at four different time instants, namely $\bar{t} = 160$, 640, 1120 and 1440, respectively. Compared with the computational simulation results in the divergent trapezoidal domain of $\theta = 20°$ (see Figs. 10.2, 10.3, 10.4 and 10.5), NAPL fingers grow much faster in the convergent trapezoidal domain of $\theta = -20°$. For example, in the case of $\bar{t} = 1440$,

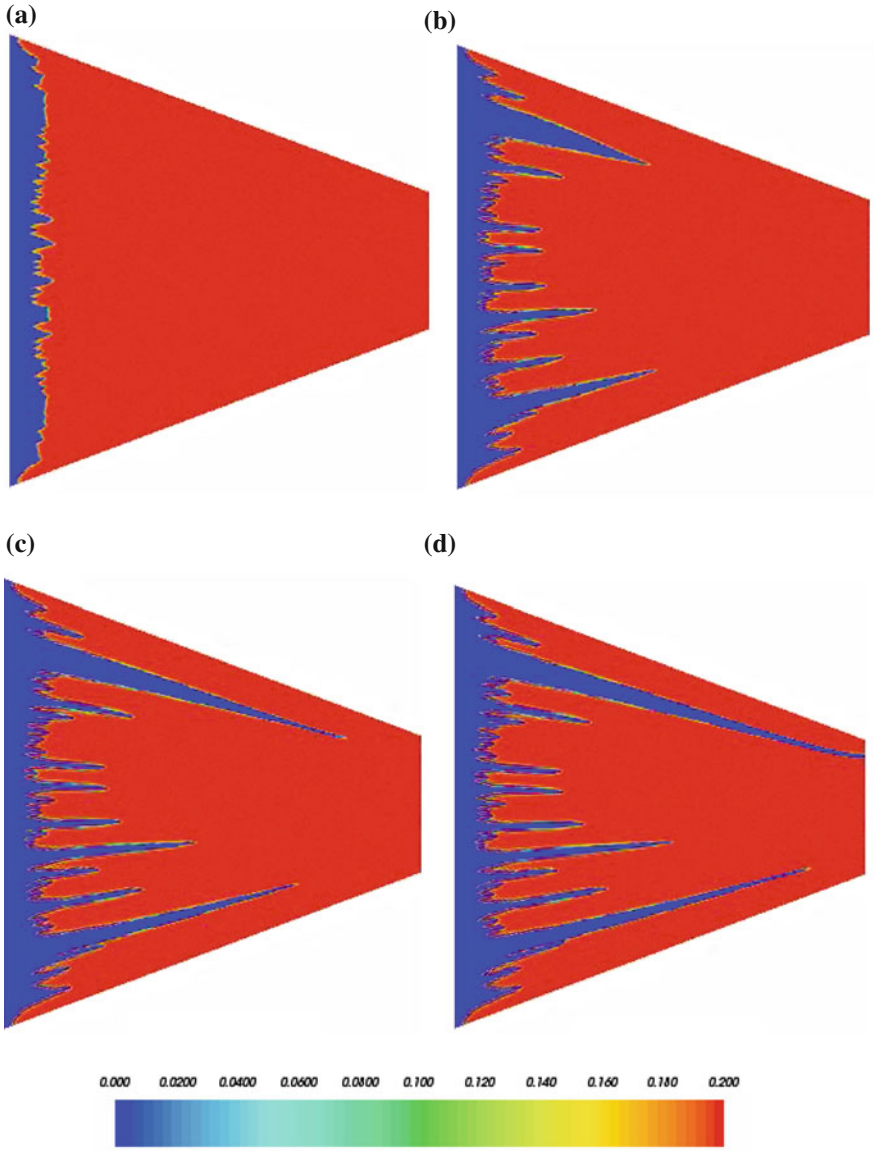

Fig. 10.7 Effects of convergent domain shape on the evolution of NAPL dissolution fronts represented by residual saturation in the fluid-saturated porous medium ($\theta = -20°$): **a** $\bar{t} = 160$; **b** $\bar{t} = 640$; **c** $\bar{t} = 1120$; **d** $\bar{t} = 1440$

one major finger has penetrated through the whole domain in the horizontal direction of the convergent trapezoidal domain in the case of $\theta = -20°$, while it only propagates about one third of the whole domain in the horizontal direction of the divergent trapezoidal domain in the case of $\theta = 20°$. This further demonstrates that domain shapes can have significant effects on the formation of NAPL

dissolution fingering in the fluid-saturated porous medium. The implication of this recognition is that in terms of land remediation, the divergent flow might be more efficient than the convergent flow because faster finger growth will lead to earlier breakthrough of clean water, which then will extend the remediation process for some period. This indicates that from the residual NAPL removal point of view, flow injection through an injection well might be more efficient than flow pumping through a pumping well.

Next, the computational model of a rectangular shape ($\theta = 0°$) is used to test the assumption that the second-order dispersion tensor can be treated as a function of the averaged linear velocity component in the inflow direction because it has been widely used in the previous theoretical analyses (Chadam et al. 1986; Imhoff and Miller 1996; Zhao et al. 2008a, b, c). For this purpose, two cases are considered in the corresponding computations. In the first case (known as the current dispersion model here), both the horizontal and vertical components of the averaged linear velocity vector are considered in the evaluation of the second-order dispersion tensor, while in the second case (known as the previous dispersion model in this investigation), only the horizontal component of the averaged linear velocity vector is considered in the evaluation of the second-order dispersion tensor. In this situation, the dimensionless lengths (i.e. $\bar{L}_x$ and $\bar{L}_{y1}$) of the computational domain are 4,713 and 3,142 in the $\bar{x}$ and $\bar{y}$ directions, while the whole computational domain is simulated by 99,301 four-node square elements of 100,000 nodal points in total. To eliminate any errors caused by finite element meshes, the finite element mesh with the same initially-perturbed residual saturation field is used for both the current and previous dispersion models. The dimensionless time-step length is 1.9 in the computational simulation. Other parameters used here is exactly the same as those used in the previous computational models of trapezoidal shapes.

Figure 10.8 shows the comparison of the simulation results for the NAPL residual saturation from the current dispersion model with those from the previous dispersion model at four different time instants, namely $\bar{t} = 190, 380, 570$ and 950, respectively. In this figure, the simulation results shown in the left column are obtained from using the current dispersion model, while the simulation results shown in the right column are obtained from using the previous dispersion model. Even though the fluid flow is, strictly speaking, no longer one-dimensional at the NAPL dissolution front (see Fig. 10.9), it can be clearly observed (from Fig. 10.8) that the morphological evolution patterns of a NAPL dissolution front predicted from the current dispersion model is almost the same as those predicted from the previous dispersion model. This demonstrates that for the NAPL dissolution-front instability problem of a rectangular domain, the previous dispersion model can produce accurate theoretical and numerical solutions for the prediction of morphological evolution patterns of NAPL dissolution fronts in fluid-saturated porous media of supercritical Zhao numbers. Except for remarkable savings in computational efforts, the major benefit of using the previous dispersion model is that it enables the theoretical analysis of this kind of instability problems to become possible (Zhao et al. 2010a).

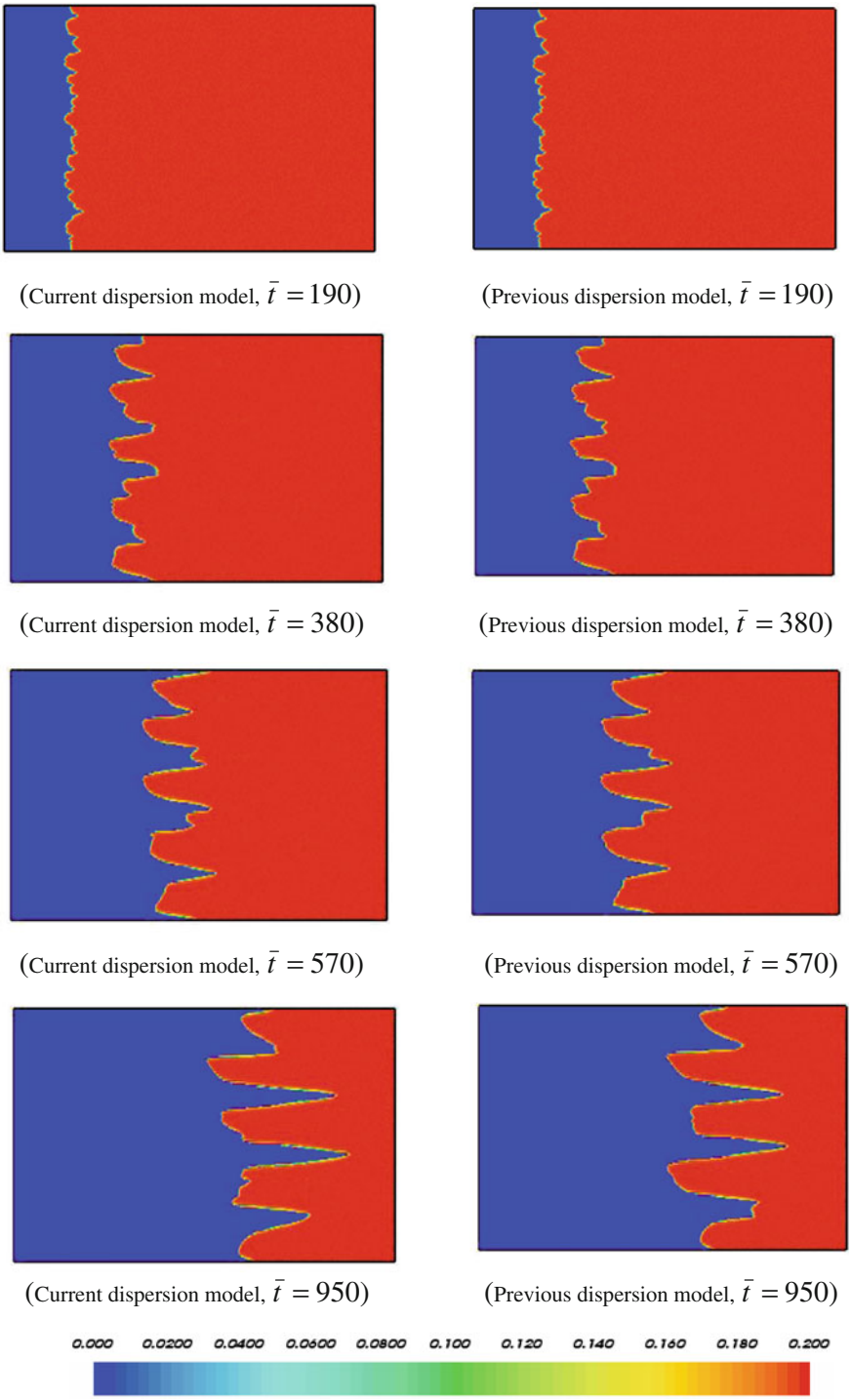

Fig. 10.8 Comparison of the simulation results from the current dispersion model with those from the previous dispersion model (NAPL residual saturation)

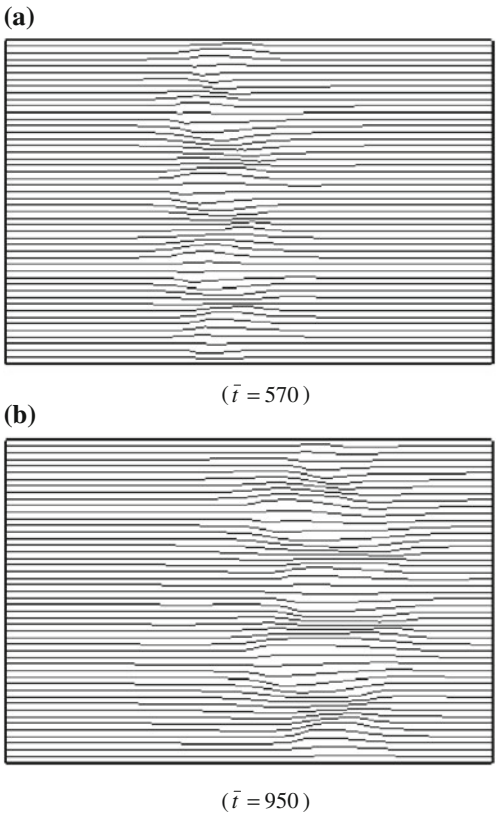

Fig. 10.9 Streamline distributions in the rectangular domain at two time instants: **a** $\bar{t} = 570$; **b** $\bar{t} = 950$

It is noted that on the basis of the numerical results shown in Figs. 10.2, 10.3, 10.4 and 10.5, it clearly indicates that the saturation of the NAPL is 0 and 0.2 behind and in front of the NAPL dissolution interface, respectively. This means that $\partial S_n/\partial t$ should be equal to zero, leading to either $S_n = 0$ (behind the NAPL dissolution interface) or $C = C_{eq}$ (in front of the NAPL dissolution interface) from Eqs. (10.1) and (10.3). As a result, the pressure gradient of the aqueous phase fluid can be equal to a nonzero constant in Eq. (10.3), from the mathematical point of view. This inference is certainly in good coincidence to the boundary condition, which states that there exists a pressure gradient of the aqueous phase fluid in the computational domain between $x = 0$ and $x = L_x$.

In summary, the related numerical simulation results have demonstrated that: (1) domain shapes have a significant effect on both the propagating speed and the morphological evolution pattern of a NAPL dissolution-front in the fluid-saturated porous medium; (2) an increase in the divergent angle of a trapezoidal domain can lead to a decrease in the propagating speed of the NAPL dissolution front; (3) the morphological evolution pattern of the NAPL dissolution-front in a rectangular domain is remarkably different from that in a trapezoidal domain of a large divergent angle; (4) for a rectangular domain, the simplified dispersion model,

which is commonly used in the theoretical analysis and numerical simulation, is valid for solving NAPL dissolution-front instability problems in fluid-saturated porous media; and (5) compared with diverging flow (when the trapezoidal domain is inclined outward), converging flow (when the trapezoidal domain is inclined inward) can enhance the growth of NAPL fingers, indicating that pump-and-treat systems by extracting contaminated groundwater might enhance NAPL dissolution fingering and lead to less uniform dissolution fronts.

10.3 Effects of Mesh Discretization Error on the Morphological Evolution of NAPL Dissolution Fronts in Supercritical Systems

Compared with the simulation of a rectangular domain, the simulation of a trapezoidal domain may involve the following two effects: (1) since the two neighbour boundaries are not perpendicular each other, the inflow perpendicular to the entrance (i.e. one side of the trapezoidal domain) may change the flow direction just when it passes the entrance of the domain. This phenomenon can be called the entrance corner effect (or just the corner effect for short). (2) Since irregular quadrilateral elements, in which two neighbour sides are not perpendicular each other, must be used to simulate the trapezoidal domain, mesh discretization including mesh inclination (i.e. grid orientation) is inevitable in the computational model. This phenomenon can be called the mesh discretization effect. The main purpose of this section is to investigate both the corner effect and mesh discretization effect on the morphological evolution of NAPL dissolution fronts in trapezoidal domains consisting of fluid-saturated porous media through conducting detailed theoretical analysis and running several computational models.

For a rectangular domain, the dimensionless pressure gradient, $\bar{p}'_{axf}$, of the aqueous phase liquid on a vertical cross-section is constant in the NAPL completely dissolved region, while for a trapezoidal domain shown in Fig. 10.10, it is a function of the location of the vertical cross-section in the NAPL completely dissolved region. From the mass conservation of the aqueous phase liquid, this function can be determined and expressed in the following form:

$$\bar{p}'_{axf} = \frac{\bar{L}_{y1}}{\bar{L}_{y1} + 2\bar{x}tg\theta}\bar{p}'_{axf0}, \tag{10.29}$$

where $\bar{p}'_{axf0}$ is the dimensionless pressure gradient of the aqueous phase on the upstream boundary; $\bar{x}$ is the location of the vertical cross-section in the NAPL completely dissolved region within the trapezoidal domain.

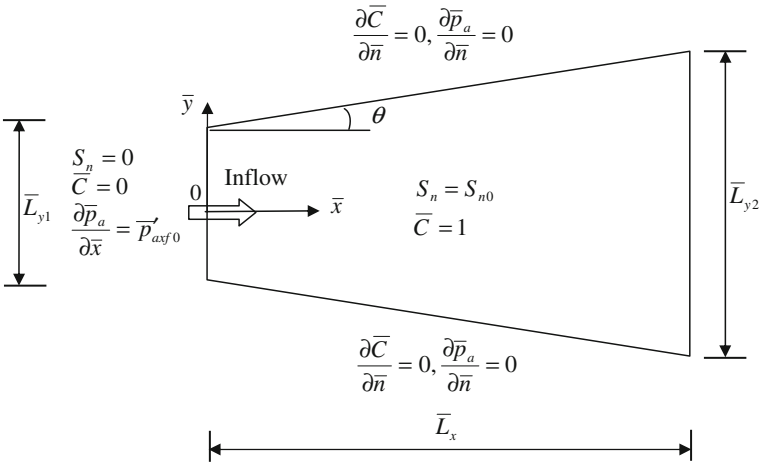

Fig. 10.10 Geometry and boundary conditions for the NAPL dissolution problem on the basis of dimensionless quantities

10.3.1 The Theoretical Basis of Mesh Discretization Error Estimation for NAPL Dissolution Problems

10.3.1.1 The Dynamic Behaviour of a NAPL Dissolution System

To facilitate the discussion of the mesh discretization error associated with the computational simulation results in the forthcoming subsections, it is necessary to briefly describe the dynamic behaviour of a NAPL dissolution system in a rectangular domain. Since the governing equations of a NAPL dissolution problem in a rectangular domain is exactly the same as those of a NAPL dissolution problem in a trapezoidal domain, the dynamic behaviour for both the rectangular domain and the trapezoidal domain should be similar so that the previous theoretical results from a rectangular domain may have some reference values when the mesh discretization error associated with the computational simulation results from a trapezoidal domain are discussed.

For the purpose of describing the dynamic behaviour of a NAPL dissolution system, the dimensionless Zhao number is defined as follows (Zhao et al. 2010c):

$$Zh = -\overline{p}'_{axf} = \frac{V_{axf}}{\sqrt{\phi \tau D_m}} \sqrt{\frac{1}{\beta_0}} = F_{advection} F_{dispersion} F_{dissolution}, \tag{10.30}$$

where V_{axf} is the Darcy velocity of the aqueous phase fluid after the NAPL is completely dissolved in the NAPL dissolution system; ϕ and τ are the porosity and tortuosity of the porous medium, respectively; D_m is the molecular diffusivity of the NAPL species in the aqueous phase; β_0 is the dissolution rate of the NAPL. It needs

to be pointed out that in Eq. (10.30), $F_{advection} = V_{axf}$, representing the aqueous phase fluid advection in the NAPL dissolution system; $F_{dispersion} = 1/\sqrt{\phi\tau D_m}$, representing the NAPL solute diffusion/dispersion in the NAPL dissolution system; and $F_{dissolution} = \sqrt{1/\beta_0}$, representing the kinetics of the NAPL dissolution. Thus the Zhao number is a comprehensive dimensionless number to represent the three major controlling mechanisms (i.e. advection, dispersion and NAPL dissolution) simultaneously taking place in the NAPL dissolution system.

When the domain of a NAPL dissolution system is rectangular, then the critical Zhao number of the system has been mathematically derived in a previous study (Zhao et al. 2010c) as follows:

$$Zh_{critical} = \frac{\left(3 - \frac{k(S_{n0})}{k(S_{nf})}\right)\left(1 + \frac{k(S_{n0})}{k(S_{nf})}\right)}{2\left(1 - \frac{k(S_{n0})}{k(S_{nf})}\right)}, \tag{10.31}$$

where $Zh_{critical}$ is the critical Zhao number of the NAPL dissolution system of a rectangular shape; $k(S_{n0})$ is the saturation-dependent permeability of the porous medium to aqueous phase flow at $S_n = S_{n0}$; $k(S_{nf})$ is the saturation-dependent permeability of the porous medium to aqueous phase flow at $S_n = S_{nf}$; $S_{nf} = 0$ is the saturation of the NAPL after it is completely dissolved in the NAPL dissolution system.

By means of both the Zhao number and the critical Zhao number, the instability of NAPL dissolution fronts in fluid-saturated porous media of rectangular domains can be assessed. Note that if the domain of a NAPL dissolution system is of a rectangular shape, then the Darcy velocity of the aqueous phase fluid after the NAPL is completely dissolved (i.e. V_{axf}) is constant, while if the domain of an NAPL dissolution system is of a trapezoidal shape, then the Darcy velocity of the aqueous phase fluid after the NAPL is completely dissolved (i.e. V_{axf}) is no longer constant. In the latter case, the instability criterion derived from the rectangular shape can be applicable, provided that an appropriate Darcy velocity of the aqueous phase fluid is selected in the NAPL dissolved region.

It is interesting to note that the Zhao number can be expressed by a combination of the Peclet number and the Thiele modulus (Hong et al. 1999). If the effective diffusion/dispersion coefficient is defined as $D_{effective} = \phi\tau D_m$, then the Thiele modulus of the dissolution system can be expressed as $Tm = L^*\sqrt{\beta_0/D_{effective}}$, where L^* is the intrinsic characteristic length of the dissolution system. Similarly, the Peclet number of the dissolution system can be expressed as $Pe = (V_{axf}L^*)/D_{effective}$. Consequently, the Zhao number of the dissolution system can be expressed as follows:

$$Zh = \left(\frac{V_{axf}L^*}{D_{effective}}\right)\left(\frac{1}{L^*}\sqrt{\frac{D_{effective}}{\beta_0}}\right) = \frac{Pe}{Tm}. \tag{10.32}$$

This indicates that the Zhao number of a NAPL dissolution system is equal to the ratio of the Peclet number to the Thiele modulus of the dissolution system. Clearly, the Peclet number can be only used to describe the interaction between the advection and diffusion/dispersion processes, while the Thiele modulus can be only used to describe the interaction between the NAPL dissolution and diffusion/dispersion processes. On the contrary, the Zhao number can be used to simultaneously describe all three processes, namely the advection, NAPL dissolution and diffusion/dispersion processes, in a NAPL dissolution system. This is the main reason why the Zhao number needs to be used to describe the overall characteristic of a NAPL dissolution system.

From the linear stability theory, the NAPL dissolution front can be expressed as (Zhao et al. 2010c):

$$S(\xi, \bar{y}, \bar{t}) = \xi - \bar{\delta}_A \exp(\bar{\omega}\bar{t}) \cos(\bar{m}\bar{y}), \tag{10.33}$$

where $\bar{\omega}$ is the dimensionless growth rate; δ_A is the amplitude of an initial small perturbation; $\bar{t}$ is the dimensionless time after the perturbation is applied to the NAPL dissolution system; $\bar{m}$ is the dimensionless wavenumber of the perturbation; ξ is the coordinate of the moving coordinate system in the $\bar{x}$ direction and can be expressed as follows:

$$\xi = \bar{x} - \bar{v}_{front}\bar{t}, \quad \bar{v}_{front} = -\frac{\bar{p}'_{axf}}{S_{n0}} = \frac{Zh}{S_{n0}}. \tag{10.34}$$

Since Eq. (10.34) indicates that the initial planar NAPL dissolution-front is always represented by $\xi = 0$, the amplitude of the finger when a NAPL dissolution system is in an unstable state (in the case of $Zh > Zh_{critical}$), can be expressed as:

$$A_{Finger} = \delta_A e^{\bar{\omega}\bar{t}}, \tag{10.35}$$

where A_{Finger} is amplitude of the finger when the NAPL dissolution system is in an unstable state.

Equation (10.35) clearly indicates that for a given time, the greater the amplitude of an initial small perturbation, the greater the amplitude of the finger. Also, for a given small perturbation, the earlier the perturbation is applied to the NAPL dissolution system, the greater the amplitude of the finger.

10.3.1.2 The Propagation Characteristic of Mesh Discretization Error and the Concept of Equivalent Initial Perturbation

As demonstrated by the previous study (Zhao et al. 2010c), the basic characteristic of a NAPL dissolution-front instability problem in a fluid-saturated porous medium is that the NAPL dissolution front divides the whole problem domain into the following two sub-domains: a NAPL un-dissolved sub-domain (in the downstream

direction of the NAPL dissolution front) and a NAPL completely-dissolved subdomain (in the upstream direction of the NAPL dissolution front). Thus, the instability of the NAPL dissolution system can only take place on the NAPL dissolution front. This is the main reason why the instability of the NAPL dissolution system is commonly called the NAPL dissolution-front instability problem. For this reason, the mesh discretization error associated with the NAPL dissolution-front instability problem can only propagate with the propagation of the NAPL dissolution front in the fluid-saturated porous medium.

To understand the propagation characteristic of the mesh discretization error associated with a NAPL dissolution-front instability problem, we consider a common boundary between several four-node rectangular elements (that are used to simulate a part of a rectangular domain) and assume that this common boundary contains N nodal points. For the sake of facilitating the analysis, we can assume that $N = 6$, as shown in Fig. 10.11. Suppose the distance between any two adjacent nodal points is equal, we can represent this distance by $\Delta\bar{x}$, so that the mesh discretization error associated with each nodal point is equal and can be expressed by δ_d. If the NAPL dissolution front is located at node 1 and the initial dimensionless time is considered as $\bar{t}_0 = 0$, then the dimensionless times can be expressed as $\bar{t}_1$, $\bar{t}_2$, $\bar{t}_3$, $\bar{t}_4$ and $\bar{t}_5$ when the NAPL dissolution front propagates from node 1 to nodes 2, 3, 4, 5, and 6 respectively. For a rectangular domain, the propagation speed (i.e. $\bar{v}_{front} = -\bar{p}'_{axf} \Big/ S_{n0} = Zh/S_{n0}$) of the NAPL dissolution front is constant (Zhao et al. 2010c), so that the time period when the NAPL dissolution front propagates between any two adjacent nodal points is also constant and can be expressed as $\Delta\bar{t}$. Thus, when the NAPL dissolution front propagates from node 1 to node 2, the mesh discretization error associated with $\Delta\bar{x}$ between nodes 1 and 2 grows and the resulting error at node 2 can be expressed as follows:

$$\delta_{d2} = \delta_d e^{\bar{\omega}\bar{t}_1} = \delta_d e^{\bar{\omega}\Delta\bar{t}}. \tag{10.36}$$

However, when the NAPL dissolution front propagates from node 2 to node 3, the total mesh discretization error associated with node 2 is equal to the sum of δ_{d2} and δ_d (i.e. the mesh discretization error associated with $\Delta\bar{x}$ between nodes 2 and 3).

$$\delta_{d2}^{total} = \delta_{d2} + \delta_d = \delta_d e^{\bar{\omega}\Delta\bar{t}} + \delta_d = \delta_d(1 + e^{\bar{\omega}\Delta\bar{t}}). \tag{10.37}$$

This means that when the NAPL dissolution front propagates from node 2 to node 3, the resulting error at node 3 can be expressed as follows:

$$\delta_{d3} = \delta_{d2}^{total} e^{\bar{\omega}\Delta\bar{t}} = \delta_d(1 + e^{\bar{\omega}\Delta\bar{t}})e^{\bar{\omega}\Delta\bar{t}} = \delta_d(e^{\bar{\omega}\Delta\bar{t}} + e^{2\bar{\omega}\Delta\bar{t}}). \tag{10.38}$$

Similarly, the resulting mesh discretization errors at nodes 4, 5 and 6 can be expressed in the following equations:

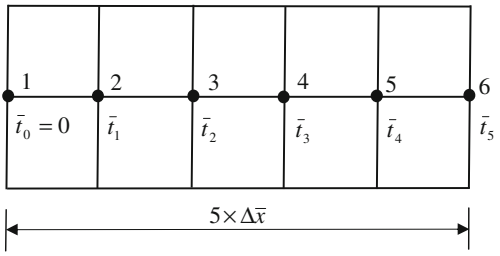

Fig. 10.11 Propagation characteristic of the mesh discretization error associated with a NAPL dissolution front propagating along the line containing 6 nodal points

$$\delta_{d4} = \delta_d(e^{\bar{\omega}\Delta\bar{t}} + e^{2\bar{\omega}\Delta\bar{t}} + e^{3\bar{\omega}\Delta\bar{t}}), \tag{10.39}$$

$$\delta_{d5} = \delta_d(e^{\bar{\omega}\Delta\bar{t}} + e^{2\bar{\omega}\Delta\bar{t}} + e^{3\bar{\omega}\Delta\bar{t}} + e^{4\bar{\omega}\Delta\bar{t}}), \tag{10.40}$$

$$\delta_{d6} = \delta_d(e^{\bar{\omega}\Delta\bar{t}} + e^{2\bar{\omega}\Delta\bar{t}} + e^{3\bar{\omega}\Delta\bar{t}} + e^{4\bar{\omega}\Delta\bar{t}} + e^{5\bar{\omega}\Delta\bar{t}}). \tag{10.41}$$

Generally, when the NAPL dissolution front propagates from node 1 to node N, the resulting mesh discretization error at node N can be expressed as follows:

$$\begin{aligned}\delta_{dN} &= \delta_d \sum_{i=1}^{N-1} e^{(N-i)\bar{\omega}\Delta\bar{t}} = \delta_d\left(\frac{e^{\bar{\omega}\Delta\bar{t}}(e^{(N-1)\bar{\omega}\Delta\bar{t}} - 1)}{e^{\bar{\omega}\Delta\bar{t}} - 1}\right) \\ &\approx \delta_d\left(\frac{e^{\bar{\omega}\Delta\bar{t}}(e^{(N-1)\bar{\omega}\Delta\bar{t}})}{e^{\bar{\omega}\Delta\bar{t}} - 1}\right) = \delta_d\left(\frac{e^{\bar{\omega}\Delta\bar{t}}}{e^{\bar{\omega}\Delta\bar{t}} - 1}\right)e^{\bar{\omega}\bar{t}} \quad (\text{for large } N)\end{aligned} \tag{10.42}$$

Note that for a fine mesh of finite elements, δ_d can be controlled to be much less than unity (i.e. $\delta_d \ll 1$), so that $(e^{(N-1)\bar{\omega}\Delta\bar{t}} - 1)$ should be much greater than unity when the finger grows to a visible size. As a result, $(e^{(N-1)\bar{\omega}\Delta\bar{t}} \gg 1)$, so that $(e^{(N-1)\bar{\omega}\Delta\bar{t}} - 1) \approx e^{(N-1)\bar{\omega}\Delta\bar{t}}$ in the process of deriving Eq. (10.42). Thus, when the NAPL dissolution front propagates from node 1 to node N, the amplitude of the finger caused by the mesh discretization error (in a rectangular domain) can be determined by the following equation:

$$A_{Finger}^{mesh} = \delta_{dN} = \delta_d \sum_{i=1}^{N-1} e^{(N-i)\bar{\omega}\Delta\bar{t}} \approx \delta_d\left(\frac{e^{\bar{\omega}\Delta\bar{t}}}{e^{\bar{\omega}\Delta\bar{t}} - 1}\right)e^{\bar{\omega}\bar{t}}, \tag{10.43}$$

where A_{Finger}^{mesh} is the amplitude of the finger caused by the mesh discretization error in the NAPL dissolution system of a rectangular domain.

Note that for a NAPL dissolution-front instability problem in a rectangular domain, the dimensionless growth rate of perturbation can be theoretically determined as follows (Zhao et al. 2010c):

$$\bar{\omega} = \frac{\bar{p}'_{axf}}{(1+\beta)S_{n0}}\left\{\frac{(1+\beta)\bar{p}'_{axf}}{1-\bar{\alpha}_L\bar{p}'_{axf}} + \left[(1+\beta) + \left(\frac{1}{1-\bar{\alpha}_L\bar{p}'_{axf}} - \bar{\alpha}_L\bar{m}\right)(1-\beta)\right]\sigma\right\} - \frac{\bar{p}'_{axf}}{(1+\beta)S_{n0}}\left[\left(\bar{m} - \frac{\bar{p}'_{axf}}{1-\bar{\alpha}_L\bar{p}'_{axf}} - \bar{\alpha}_L\bar{m}^2\left(1-\bar{\alpha}_L\bar{p}'_{axf}\right)\right)\frac{(1-\beta)}{1-\bar{\alpha}_L\bar{p}'_{axf}}\right], \tag{10.44}$$

$$\sigma = \frac{\sqrt{\left(\frac{\bar{p}'_{axf}}{1-\bar{\alpha}_L\bar{p}'_{axf}}\right)^2 + \frac{4\bar{m}^2(1-\bar{\alpha}_T\bar{p}'_{axf})}{1-\bar{\alpha}_L\bar{p}'_{axf}}} - \frac{\bar{p}'_{axf}}{1-\bar{\alpha}_L\bar{p}'_{axf}}}{2}, \tag{10.45}$$

where $\bar{p}'_{axf}$ is the dimensionless pressure gradient of the aqueous phase liquid on a vertical cross-section in the NAPL completely dissolved region; S_{n0} is the initial saturation of the NAPL; $\bar{\alpha}_T$ and $\bar{\alpha}_L$ are the dimensionless transversal and longitudinal dispersivities of the NAPL species in the aqueous phase; β is the ratio of the permeability of the NAPL un-dissolved region to that of the NAPL completely-dissolved region; $\bar{m}$ is the dimensionless wavenumber of the perturbation.

Equations (10.43)–(10.45) clearly indicate that if the mesh discretization error associated with the NAPL dissolution instability system of a rectangular domain is known, then the amplitude of the finger caused by the mesh discretization error (in a rectangular domain) can be theoretically determined. Unfortunately, the main purpose of this study is to find the mesh discretization error associated with the NAPL dissolution instability system, so that an inverse problem needs to be solved. This means that if the amplitude of the finger caused by the mesh discretization error (in a rectangular domain) is numerically evaluated, then the mesh discretization error associated with the NAPL dissolution instability system of a rectangular domain can be determined using the following equation:

$$\delta_d = \frac{A^{mesh}_{Finger}}{\sum_{i=1}^{N-1} e^{(N-i)\bar{\omega}\Delta\bar{t}}} \approx A^{mesh}_{Finger}\left(\frac{e^{\bar{\omega}\Delta\bar{t}}-1}{e^{\bar{\omega}\Delta\bar{t}}}\right)e^{-\bar{\omega}\bar{t}}. \tag{10.46}$$

Although Eq. (10.46) is not easy to be evaluated, it provides a theoretical basis for estimating the mesh discretization error associated with the NAPL dissolution instability system of a rectangular domain.

To solve this inverse problem better, the concept of equivalent initial perturbation associated with the mesh discretization error of a NAPL dissolution system is presented below. The basic idea behind the concept of equivalent initial perturbation associated with the mesh discretization of a NAPL dissolution system is that the amplitude of the finger caused by the mesh discretization error can be approximately represented by the following equation:

$$A_{Finger}^{mesh} = \delta_d^{equivalent} e^{\bar{\omega}\bar{t}}, \tag{10.47}$$

where $\delta_d^{equivalent}$ is the equivalent initial perturbation associated with the mesh discretization error of a NAPL dissolution system.

Considering Eqs. (10.43) and (10.47) simultaneously yields the following equation:

$$\delta_d^{equivalent} = \frac{\delta_d}{e^{\bar{\omega}\bar{t}}} \sum_{i=1}^{N-1} e^{(N-i)\bar{\omega}\Delta\bar{t}} \approx \delta_d \left(\frac{e^{\bar{\omega}\Delta\bar{t}}}{e^{\bar{\omega}\Delta\bar{t}} - 1} \right) = \alpha\delta_d, \quad \alpha = \frac{e^{\bar{\omega}\Delta\bar{t}}}{e^{\bar{\omega}\Delta\bar{t}} - 1}. \tag{10.48}$$

Equation (10.48) indicates that since $\bar{\omega}\Delta\bar{t}$ is a constant (as demonstrated later), the equivalent initial perturbation associated with the mesh discretization error of a NAPL dissolution system is also a constant and theoretically computable. Since δ_d remains unknown in this equation, Eq. (10.47) is directly used to calculate the equivalent initial perturbation associated with the mesh discretization error of a NAPL dissolution system in Sect. 10.3.2. Therefore, Eq. (10.47) may be considered as the core of the proposed finger-amplitude growing theory associated with the mesh discretization error in the NAPL dissolution system.

10.3.1.3 The Product of $\bar{\omega}\Delta\bar{t}$ Associated with the NAPL Dissolution System of a Trapezoidal Domain

The proposed propagation theory of mesh discretization error associated with the NAPL dissolution system of a rectangular domain can be also extended to the mesh discretization error estimation associated with the NAPL dissolution system of a trapezoidal domain. For this purpose, we can approximately divide the trapezoidal domain into a series of rectangular sub-domains. Obviously, if the number of these rectangular sub-domains approaches infinity, then the shape of the trapezoidal domain could be accurately represented. This is equivalently to use the limit concept in mathematics. However, for each rectangular sub-domain of the same dimensionless width (i.e. $\Delta\bar{x}$) in the horizontal direction, as shown in Fig. 10.12, the dimensionless pressure gradient, $\bar{p}'_{axf}$, of the aqueous phase liquid on its left-hand-side vertical boundary, which is assumed to be the current location of the NAPL dissolution front in the trapezoidal domain, is no longer constant, as indicated by Eq. (10.29) in the previous section. This means that the propagation speed (i.e. $\bar{v}_{front} = -\bar{p}'_{axf} \Big/ S_{n0}$) of the NAPL dissolution front in each rectangular sub-domain is also no longer constant. This is one of the main differences between the NAPL dissolution system of a rectangular domain and that of a trapezoidal domain.

For the purpose of determining the product of $\bar{\omega}\Delta\bar{t}$ associated with the NAPL dissolution system of a trapezoidal domain, we need to consider a typical rectangular sub-domain shown in Fig. 10.12. For this rectangular sub-domain, the time

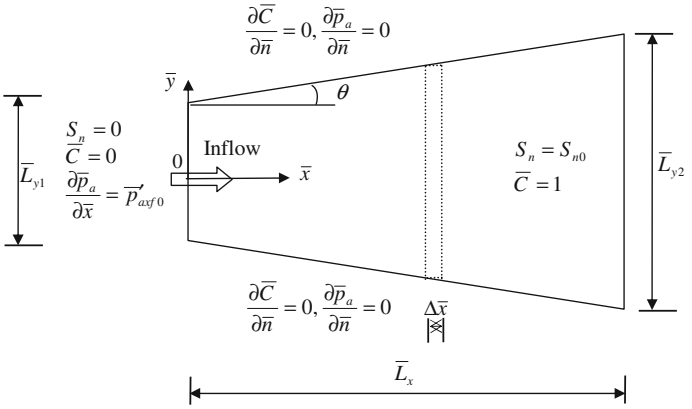

Fig. 10.12 A typical sub-domain of rectangular shape in the trapezoidal domain

period (i.e. $\Delta\bar{t}$), when the NAPL dissolution front propagates from its left-hand-side vertical boundary to its right-hand-side vertical boundary, can be expressed as follows:

$$\Delta\bar{t} = \frac{\Delta\bar{x}}{\bar{v}_{front}} = -\frac{\Delta\bar{x}S_{n0}}{\bar{p}'_{axf}} = -\frac{(\bar{L}_{y1} + 2\bar{x}tg\theta)\Delta\bar{x}S_{n0}}{\bar{L}_{y1}\bar{p}'_{axf0}}. \tag{10.49}$$

To determine the dimensionless growth rate (i.e. $\bar{\omega}$) in the typical rectangular sub-domain shown in Fig. 10.12, we need to use Eq. (10.44) to investigate how the dimensionless growth rate varies with the dimensionless pressure gradient, $\bar{p}'_{axf}$, of the aqueous phase liquid on its left-hand-side vertical boundary. Figure 10.13 shows the variation of the dimensionless growth rate with the Zhao number due to different dimensionless wavenumbers in the NAPL dissolution problem. In this figure, $Zh = -\bar{p}'_{axf}$ by definition. It is obvious that for a given dimensionless wavenumber, the dimensionless growth rate varies linearly with the Zhao number of the NAPL dissolution system.

Thus, Eq. (10.44) can be approximately rewritten in the following simplified form:

$$\bar{\omega} \approx -\bar{p}'_{axf} f(S_{n0},\ \bar{\alpha}_L,\ \bar{\alpha}_T,\ \beta) = -\frac{\bar{L}_{y1}}{\bar{L}_{y1} + 2\bar{x}tg\theta}\bar{p}'_{axf0} f(S_{n0},\ \bar{\alpha}_L,\ \bar{\alpha}_T,\ \beta), \tag{10.50}$$

where f is a function of S_{n0}, $\bar{\alpha}_L$, $\bar{\alpha}_T$ and β. This function represents the constant slope of the straight line. Thus, $f(S_{n0},\ \bar{\alpha}_L,\ \bar{\alpha}_T,\ \beta)$ should be independent of the geometrical shape of the problem domain.

Note that for the NAPL dissolution system of a rectangular domain, the value of θ is equal to zero, so that the product of $\bar{\omega}\Delta\bar{t}$ in the case of the NAPL dissolution front propagating in a rectangular domain can be expressed as follows:

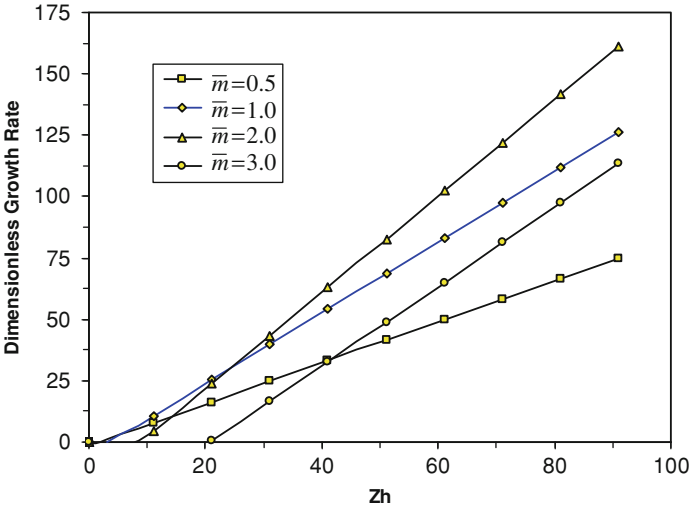

Fig. 10.13 Variation of the dimensionless growth rate with the Zhao number due to different dimensionless wavenumbers in the NAPL dissolution problem

$$(\bar{\omega}\Delta\bar{t})_{rectangular} = \Delta\bar{x}S_{n0}f(S_{n0},\ \bar{\alpha}_L,\ \bar{\alpha}_T,\ \beta). \tag{10.51}$$

Similarly, considering Eqs. (10.49) and (10.50) simultaneously yields the following product for the NAPL dissolution front propagating in a trapezoidal domain.

$$\begin{aligned}(\bar{\omega}\Delta\bar{t})_{trapezoidal} &= \left(-\frac{\bar{L}_{y1}}{\bar{L}_{y1}+2\bar{x}tg\theta}\bar{p}'_{axf0}f(S_{n0},\ \bar{\alpha}_L,\ \bar{\alpha}_T,\ \beta)\right)\times\left(-\frac{(\bar{L}_{y1}+2\bar{x}tg\theta)\Delta\bar{x}S_{n0}}{\bar{L}_{y1}\bar{p}'_{axf0}}\right)\\ &= \Delta\bar{x}S_{n0}f(S_{n0},\ \bar{\alpha}_L,\ \bar{\alpha}_T,\ \beta)\end{aligned} \tag{10.52}$$

Equations (10.51) and (10.52) indicate that although both the dimensionless growth rate (i.e. $\bar{\omega}$) and the time period (i.e. $\Delta\bar{t}$) when the NAPL dissolution front propagates the same horizontal distance (i.e. $\Delta\bar{x}$) are totally different, their products are exactly the same for the NAPL dissolution-front propagation in both the rectangular and trapezoidal domains. When the NAPL dissolution front propagates through N elements with the equal dimensionless width of $\Delta\bar{x}$, it can be easily proven that the product of $N\bar{\omega}\Delta\bar{t}$, where N is a positive integer of any value, is also exactly the same for the NAPL dissolution front propagation in both the rectangular and trapezoidal domains. This theoretical finding demonstrates that if the horizontal width of the finite elements that is used to simulate a trapezoidal domain is exactly the same as that is used to simulate a rectangular domain, the mesh discretization error propagation theory presented for the rectangular domain (in Sect. 10.3.1.2) can be, in principle, used to estimate the mesh discretization error associated with the NAPL dissolution-front propagation in the trapezoidal domain.

Thus, Eq. (10.47) is also valid for estimating the mesh discretization error associated with the NAPL dissolution-front propagation in the trapezoidal domain. This is another reason why we consider a trapezoidal domain in this investigation.

10.3.1.4 The Corner Effect at the Entrance of a Trapezoidal Domain

For a trapezoidal domain, as shown in Fig. 10.10, the two neighbour boundaries are not perpendicular each other, so that the inflow perpendicular to the entrance (i.e. one side of the trapezoidal domain) may change the flow direction just when it passes the entrance of the domain. Due to this special kind of shape, the overall flow pattern turns into a radial flow pattern at some distance away from the entrance of the flow. This means that such a corner effect can be treated as an equivalent perturbation that is just applied at the corner points of the flow entrance in the trapezoidal domain. Following the same procedures as those used in Sect. 10.3.1.2, the amplitude of the finger caused by the corner effect can be approximately represented by the following equation:

$$A_{Finger}^{corner} = \delta_c^{equivalent} e^{\bar{\omega}\bar{t}}, \tag{10.53}$$

where $\delta_c^{equivalent}$ is the equivalent initial perturbation associated with the corner effect at the entrance of a NAPL dissolution system; A_{Finger}^{corner} is the amplitude of the finger caused by the corner effect.

As a counterpart of Eq. (10.47), Eq. (10.53) may be considered as the core of the proposed finger-amplitude growing theory associated with the corner effect in the NAPL dissolution system of a trapezoidal domain. Consequently, the total amplitude of the finger (caused by both the corner effect and the mesh discretization error), which grows at either the top or the bottom boundary of the trapezoidal domain, should be equal to the sum of Eqs. (10.47) and (10.53) as follows:

$$A_{Finger}^{corner+mesh} = (\delta_c^{equivalent} + \delta_d^{equivalent}) e^{\bar{\omega}\bar{t}}. \tag{10.54}$$

where $A_{Finger}^{corner+mesh}$ is the total amplitude of the finger caused by both the corner effect and the mesh discretization error at either the top or the bottom boundary of the trapezoidal domain.

10.3.2 Corner and Mesh Discretization Effects on the Morphological Evolution of NAPL Dissolution Fronts in Supercritical Systems of Trapezoidal Domains

As shown in Fig. 10.10 in the previous section, the geometrical shape of a trapezoidal computational domain, which is symmetrical to the $\bar{x}$ axis, can be

represented by the divergent angle (i.e. θ) between a horizontal line and the top boundary. This angle is defined as a geometrical parameter in the corresponding computations. If θ is equal to zero, then the trapezoidal domain degenerates to a rectangular one.

On the basis of the previous experimental measurement results that were calibrated by several laboratory tests (Imhoff and Miller 1996; Imhoff et al. 1996; Miller et al. 1998), the following parameters are selectively used in the corresponding computational models: the initial saturation (S_{n0}) of the NAPL is 0.2; the irreducible saturation (S_{ai}) of the aqueous phase fluid is 0.15; the dimensionless longitudinal and transverse dispersivities ($\bar{\alpha}_L$ and $\bar{\alpha}_T$) are 0.2 and 0.02, respectively; the ratio (ε) of the equilibrium concentration of the NAPL species in the aqueous phase fluid to the density of the NAPL itself is 0.001; the density ratio ($\bar{\rho}_a$) of the aqueous phase fluid to the NAPL is 1.0/1.46; the value of β_1 is 0.87. To simulate the propagation of NAPL dissolution fronts appropriately, the whole computational domain is simulated by 120,000 four-node quadrilateral elements of 120,701 nodal points in total. Figure 10.14 shows the meshes of finite elements used for modeling both the rectangular domain (i.e. $\theta = 0°$) and the trapezoidal domain (i.e. $\theta = 20°$). Note that each element in this figure is further divided into 100 finer elements before the computation.

For the purpose of investigating the instability of a NAPL dissolution system, it is common practice to perturb the homogeneous distribution field of the initial NAPL saturation (S_{n0}) with a small amount (Zhao et al. 2010c). For this reason, the initial residual saturation field of the NAPL is randomly perturbed by a small amount of 1 % of the originally-input saturation of the NAPL (i.e. $S_{n0} = 0.2$) before running the computational model. This means that the initial homogeneous distribution field of the NAPL saturation (S_{n0}) is replaced and reassigned by a slightly perturbed non-homogeneous distribution field of the NAPL saturation before running the computational model. The dimensionless length (i.e. $\bar{L}_x$) of the computational domain is 6,284 in the $\bar{x}$ direction, while the dimensionless length (i.e. $\bar{L}_{y1}$) of the left boundary is fixed to 3,142 and 2,046 in the $\bar{y}$ direction for two different computational domains, namely $\theta = 0°$ and 20°, respectively. The Zhao number used for the two computational models (at the entrance of the flow) is 1.0, while the dimensionless time-step length is 3.2.

10.3.2.1 Corner and No-Flow Boundary Effects of Computational Domains

Figure 10.15 shows the morphological evolution of NAPL dissolution fronts in both the rectangular ($\theta = 0°$) and the trapezoidal ($\theta = 20°$) domains consisting of the fluid-saturated porous media at two different time instants, namely $\bar{t} = 160$ and 1600, respectively. In this figure, the residual saturation of a NAPL is used to represent the NAPL dissolution front. It is observed that the NAPL dissolution front propagates much faster along the top and bottom boundaries, especially in the trapezoidal domain. This may be caused by both the no-flow boundary and

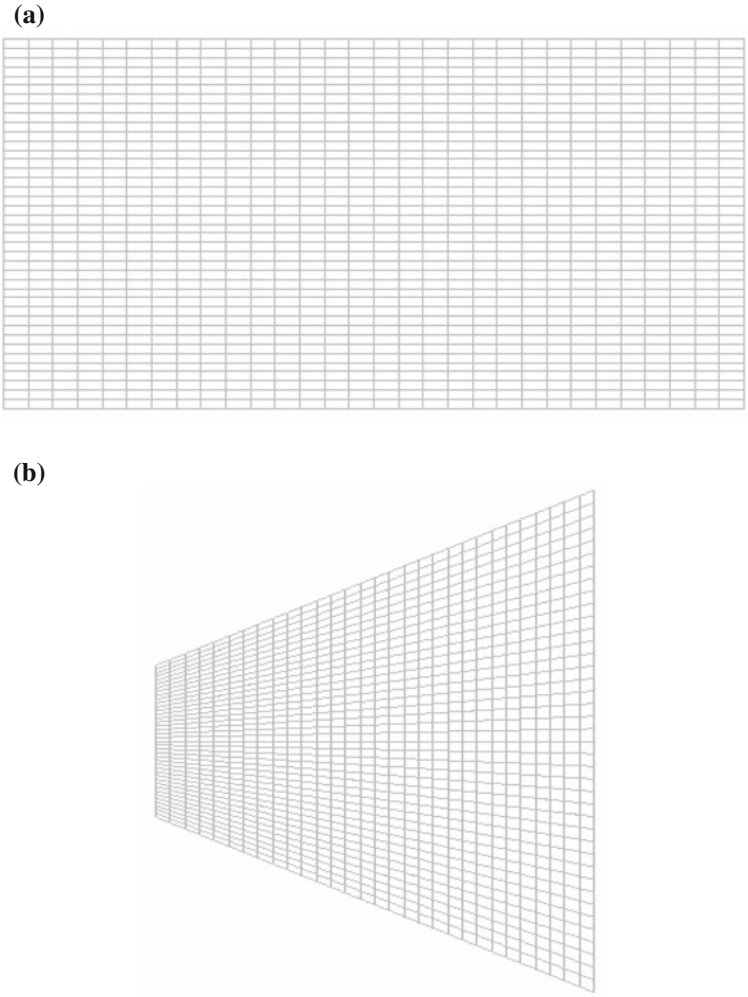

Fig. 10.14 Finite element meshes used for simulating the NAPL dissolution problem: **a** Rectangular domain; **b** Trapezoidal domain

corner effects. In the case of a rectangular domain, Kalia and Balakotaiah (2009) observed the same phenomenon in the numerical simulation of acid dissolution induced wormhole formation in carbonates. Regarding the physical reason to cause this phenomenon, they made the following explanation: "When no-flow boundaries are present in a system, an inconsistency may occur at these boundaries because of Darcy's law. As the fluid is injected in the medium, it is transported in both the axial and transverse directions. Darcy's law allows for streamwise or axial flow at the boundaries although the transverse velocity component is zero because of the boundary conditions. This leads to a deflection of the fluid carried by the

perpendicular velocity component at the boundaries to the axial direction resulting in a velocity slip. This leads to more fluid going to the boundaries and in turn resulting in relatively higher dissolution at the boundaries." Thus, the no-flow boundary effect is not a numerical artifact and has previously been mentioned for the viscous fingering phenomenon where a less viscous fluid displaces a more viscous one (Morris and Ball 1990; Yang and Yortsos 1998). Although this explanation may be valid for the flow in a rectangular domain, it cannot be used to explain why the NAPL dissolution front propagates much faster along the top and bottom boundaries in the trapezoidal domain (i.e. $\theta = 20°$). Nevertheless, this phenomenon can be better explained using the proposed finger-amplitude growing theory associated with the corner effect at the entrance of a trapezoidal domain (in Sect. 10.3.1.4). In the case of the rectangular domain (where no corner effect exists) and $\bar{t} = 1600$ (in Fig. 10.15), the amplitude of the finger at either the top or the bottom boundary is of the same order of magnitude as that of the finger within the interior of the rectangular domain. However, in the case of the trapezoidal domain (where there exists the corner effect) and $\bar{t} = 1600$ (in Fig. 10.15), the amplitude of the finger at either the top or the bottom boundary is much greater than that of the finger within the interior of the trapezoidal domain. This demonstrated that the proposed finger-amplitude growing theory associated with the corner effect at the entrance of a trapezoidal domain is useful for correctly explaining why the finger at either the top or the bottom boundary grows much faster than that within the interior of the trapezoidal domain.

10.3.2.2 Mesh Discretization Effects of Computational Domains

When the finite element and finite difference methods are used to solve the NAPL dissolution problem in a fluid-saturated porous medium, the continuum domain of the problem needs to be discretized into many elements, so that the dimensionless governing equations (i.e. the partial differential equations) of the system can be approximately represented by a set of algebraic equations. This discretization process will cause the mesh discretization error, which may result in numerical diffusion during the numerical computation. Compared with the use of rectangular and square elements in the simulation of a rectangular domain, the use of general quadrilateral elements in the simulation of a trapezoidal domain can cause extra mesh discretization error (or extra numerical diffusion) due to the involvement of mesh inclination (i.e. grid orientation). For this reason, the total diffusion/dispersion tensor of the computational model for simulating the NAPL dissolution problem in a trapezoidal domain is equal to the sum of the physical diffusion/dispersion tensor and the numerical diffusion/dispersion tensor. Since the numerical diffusion/dispersion tensor is caused by the mesh discretization error, it is desirable to reduce the numerical diffusion/dispersion tensor so that the computational simulation result can converge to the physical solution.

To examine the effect of numerical diffusion/dispersion due to mesh discretization error on the computational simulation of a NAPL dissolution problem in a

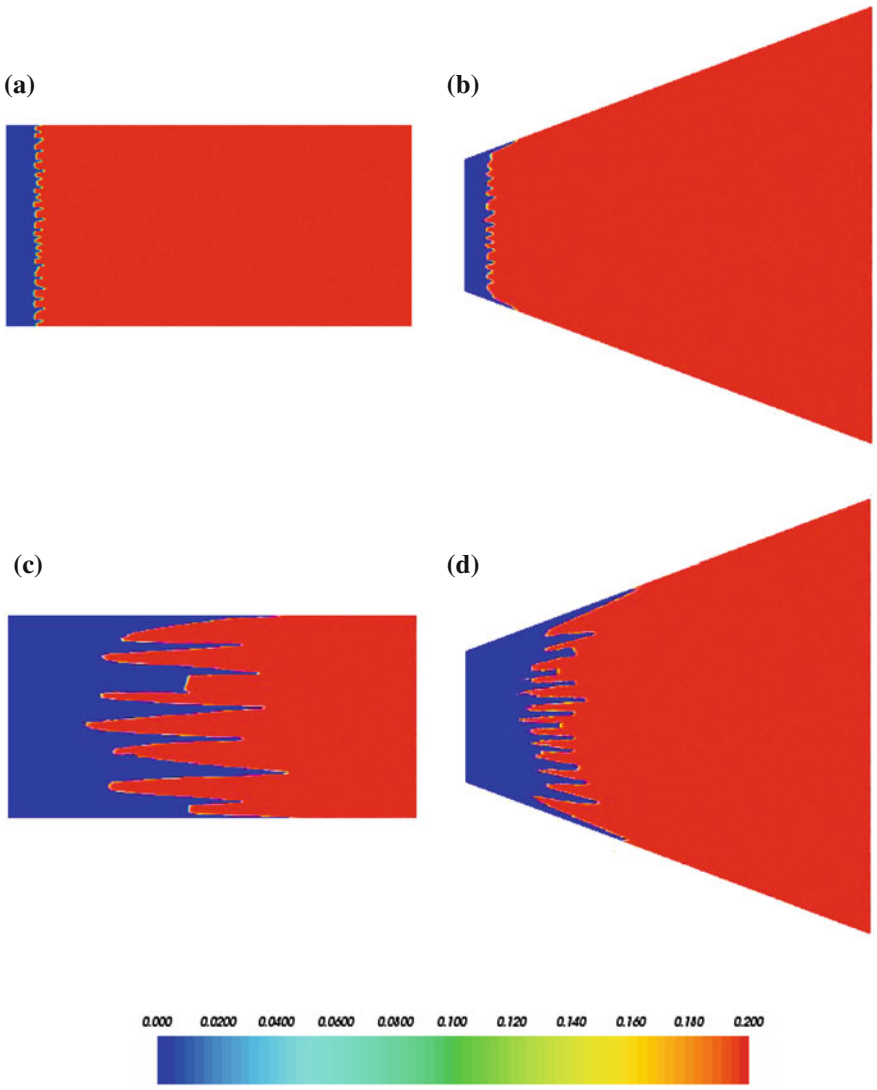

Fig. 10.15 Effects of corner and no-flow boundary on the evolution of NAPL dissolution fronts in the fluid-saturated porous medium (Supercritical system): **a** $\theta = 0, \bar{t} = 160$; **b** $\theta = 20°$, $\bar{t} = 160$; **c** $\theta = 0, \bar{t} = 1600$; **d** $\theta = 20°, \bar{t} = 1600$

trapezoidal domain, it is necessary to understand the constituents of the physical diffusion/dispersion tensor in a NAPL dissolution system. For this purpose, the physical diffusion/dispersion tensor in the NAPL dissolution system can be expressed in the following dimensional form:

$$\mathbf{D_h} = \mathbf{D_{h1}} + \mathbf{D_{h2}} = \begin{bmatrix} \tau D_m & 0 \\ 0 & \tau D_m \end{bmatrix} + \begin{bmatrix} \alpha_L \frac{v_{ax}^2}{v_a} + \alpha_T \frac{v_{ay}^2}{v_a} & (\alpha_L - \alpha_T) \frac{v_{ax} v_{ay}}{v_a} \\ (\alpha_L - \alpha_T) \frac{v_{ax} v_{ay}}{v_a} & \alpha_L \frac{v_{ay}^2}{v_a} + \alpha_T \frac{v_{ax}^2}{v_a} \end{bmatrix}, \tag{10.55}$$

where τ is the tortuosity of the porous medium; D_m is the molecular diffusivity of the NAPL species in the aqueous phase; v_{ax} and v_{ay} are the averaged linear velocity components in the x and y directions, respectively; α_T and α_L are the transversal and longitudinal dispersivities of the NAPL species in the aqueous phase; v_a is the amplitude of the averaged linear velocity vector of the aqueous phase as follows:

$$v_a = \sqrt{v_{ax}^2 + v_{ay}^2}. \tag{10.56}$$

Equation (10.55) indicates that the total physical diffusion/dispersion tensor in a NAPL dissolution system can be divided into two parts: an isotropic part (i.e. $\mathbf{D_{h1}}$) and an anisotropic part (i.e. $\mathbf{D_{h2}}$). Since the anisotropic part is directly proportional to the flow velocity, it can only vanish when there is no flow in the system. Otherwise, both the isotropic part and the anisotropic part of the total physical diffusion/dispersion tensor will exist in the NAPL dissolution system, no matter whether the problem domain is rectangular or trapezoidal. This means that even though mesh discretization error in a trapezoidal domain might cause an anisotropic numerical diffusion/dispersion tensor, the computational simulation results should converge to the physical solution, as long as the anisotropic numerical diffusion/dispersion tensor due to mesh discretization is much smaller than the total physical diffusion/dispersion tensor in the NAPL dissolution system. Although it is very difficult, if not impossible, to quantitatively evaluate the anisotropic numerical diffusion/dispersion tensor associated with mesh discretization error, it is possible to qualitatively judge its effect on the computational simulation through comparing the simulation results with the theoretical expectations, as discussed later.

In the computational simulation, the mesh discretization error decreases with the decrease of the grid size, so that numerical diffusion/dispersion can be minimized by choosing the grid size appropriately (Zhao et al. 2011). When the numerical results, which are obtained from the mesh of a given grid size, agree well with the corresponding analytical solutions and experimental results, the numerical diffusion/dispersion is considered to be minimum, compared with the physical diffusion/dispersion of the problem. To examine mesh discretization effects on the numerical results, we have simulated a subcritical NAPL dissolution system in the trapezoidal domain. In this case, the Zhao number used for the computational model (at the entrance of the flow) is reduced from 1.0 to 0.01, while the dimensionless time-step length is increased from 3.2 to 32. Figure 10.16 shows the corresponding computational simulation results. As expected theoretically (Tan and Homsy 1987), the NAPL dissolution front converges to the arc shape, which is controlled by the

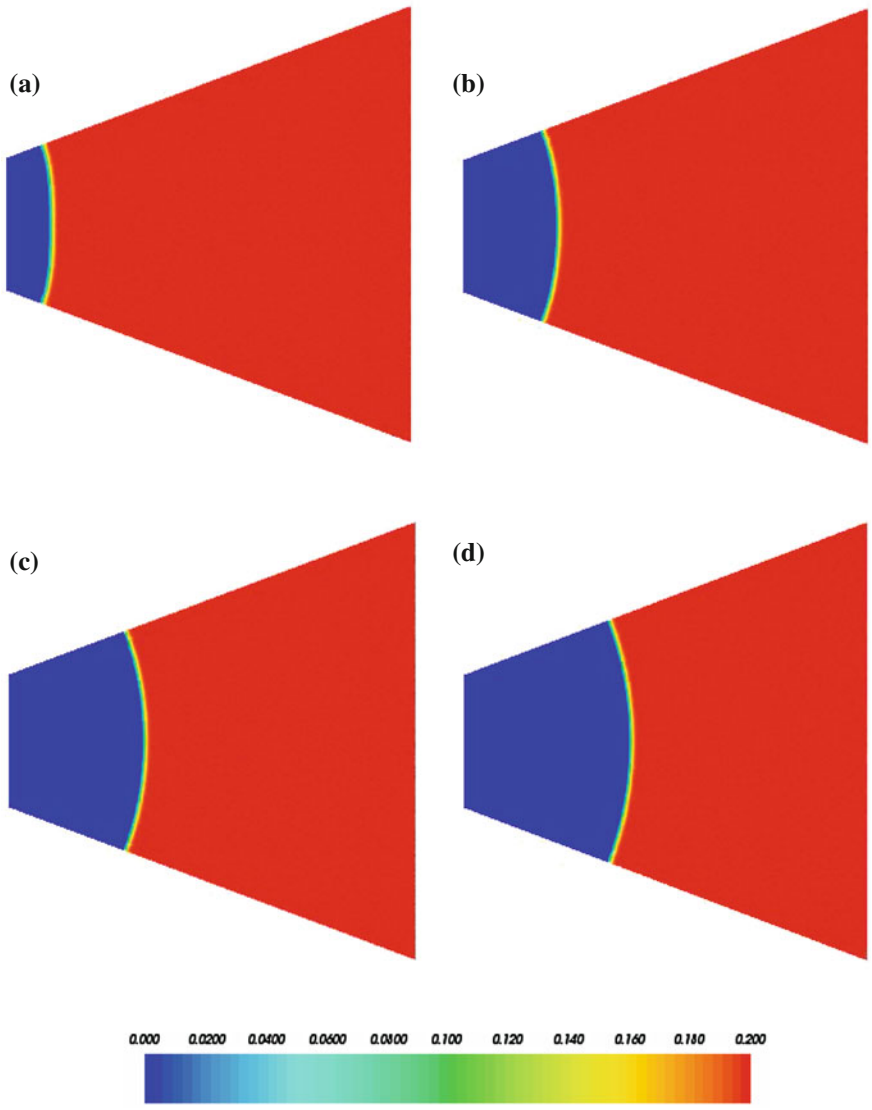

Fig. 10.16 The evolution of NAPL dissolution fronts in the trapezoidal domain consisting of the fluid-saturated porous medium (Subcritical system): **a** $\theta = 20°, \bar{t} = 320$; **b** $\theta = 20°, \bar{t} = 1600$; **c** $\theta = 20°, \bar{t} = 3200$; **d** $\theta = 20°, \bar{t} = 4800$

dynamic behaviour of the subcritical NAPL dissolution system. This is clearly evidenced in the computational simulation results. Since the numerical results have good agreement with the related theoretical expectation for the subcritical NAPL dissolution systems of trapezoidal domains, it can be concluded that the mesh discretization effect is negligible in the computational simulations of subcritical

NAPL dissolution systems. This means that the computational model used in this investigation can produce reliable numerical results for simulating subcritical NAPL dissolution systems in the trapezoidal domain consisting of a fluid-saturated porous medium. However, to examine whether the computational model used in this investigation is suitable for simulating the supercritical NAPL dissolution system of a trapezoidal domain, it is necessary to estimate the mesh discretization error of the supercritical NAPL dissolution system through using both the proposed propagation theory of mesh discretization error and the proposed finger-amplitude growing theory associated with the mesh discretization error in the NAPL dissolution system of a trapezoidal domain.

10.3.2.3 Approximate Estimation of the Mesh Discretization Error

In terms of estimating the discretization error of a numerical method, it is common practice to compare the numerical solution with the corresponding analytical solution (if any) or benchmark solution that is obtained using a very fine mesh (Zhao and Steven 1996a, b, c). Unfortunately, such practice works well for subcritical NAPL dissolution systems, but does not work for supercritical NAPL dissolution systems. This is because in the latter case, the related analytical solution is not available at all. In addition, the related benchmark solution of a supercritical NAPL dissolution system is hardly to be obtained for the following two main reasons: (1) the numerical solution of a supercritical NAPL dissolution system is strongly dependent on the perturbation applied to the system; and (2) any two different meshes (i.e. a coarse mesh and a fine mesh) of a system will result in different perturbations so that their numerical solutions lose the common ground for comparison. To overcome this difficulty, it is necessary to find a new way to approximately estimate the mesh discretization error of a supercritical NAPL dissolution system in this study.

Based on the proposed finger-amplitude growing theory associated with the mesh discretization error in the NAPL dissolution system of a trapezoidal domain, it is possible to approximately estimate the discretization error of the system through using Eq. (10.47) that is presented in the previous section. The specific procedure associated with the approximate estimation of the discretization error can be divided into the following three steps. The first step is to determine the dimensionless growth rate of the supercritical NAPL dissolution system. This can be done through considering the amplitudes of the fingers at two early computational simulation steps. For example, if the amplitudes of the finger are $A_{1Finger} = \delta_A e^{\bar{\omega}\bar{t}_1}$ and $A_{2Finger} = \delta_A e^{\bar{\omega}\bar{t}_2}$ at $\bar{t} = \bar{t}_1$ and $\bar{t} = \bar{t}_2$ respectively, then the ratio of these two amplitudes can be expressed as follows:

$$R_1 = \frac{A_{2Finger}}{A_{1Finger}} = e^{\bar{\omega}(\bar{t}_2 - \bar{t}_1)}. \tag{10.57}$$

From Eq. (10.57), the dimensionless growth rate of the supercritical NAPL dissolution system can be obtained as follows:

$$\bar{\omega} = \frac{\ln R_1}{\bar{t}_2 - \bar{t}_1}. \tag{10.58}$$

The second step is to determine the amplitude ratio of the equivalent initial perturbation (due to the discretization error) to the total initial perturbation in the supercritical NAPL dissolution system. In this situation, the discretization error is viewed as an equivalent initial perturbation, which can be determined from the computational simulation results of a supercritical NAPL dissolution system in which no any other initial perturbation is applied. On the other hand, the total initial perturbation, which is the sum of the equivalent initial perturbation (due to the discretization error) and the applied initial perturbation (due to some physical considerations), can be determined from the computational simulation results of a supercritical NAPL dissolution system in which an initial perturbation (due to some physical considerations) is applied. If the amplitudes of the fingers are $A_{1Finger} = \delta_{A1} e^{\bar{\omega}\bar{t}_1}$ (at $\bar{t} = \bar{t}_1$) for the supercritical NAPL dissolution system without any other initial perturbation applied and $A_{2Finger} = \delta_{A2} e^{\bar{\omega}\bar{t}_2}$ (at $\bar{t} = \bar{t}_2$) for the supercritical NAPL dissolution system with an initial perturbation applied, then the amplitude ratio of the equivalent initial perturbation (due to the discretization error) to the total initial perturbation can be evaluated under the condition of $A_{1Finger} = A_{2Finger}$. This can result in the following formula:

$$R_2 = \frac{\delta_{A1}}{\delta_{A2}} = e^{\bar{\omega}(\bar{t}_2 - \bar{t}_1)}, \tag{10.59}$$

where δ_{A1} is the amplitude of the equivalent initial perturbation due to the discretization error; δ_{A2} is the amplitude of the total initial perturbation.

The third step is to determine the amplitude of the equivalent initial perturbation due to the discretization error in the supercritical NAPL dissolution system. Since the initially applied perturbation is known, it can be represented by $\delta_{Ainitial}$, so that $\delta_{A2} = \delta_{Ainitial} + \delta_{A1}$. With consideration of Eq. (10.59), this leads to the following formula for evaluating δ_{A1}:

$$\delta_{A1} = \frac{R_2}{1 - R_2} \delta_{Ainitial}. \tag{10.60}$$

Based on the proposed procedure above, we have rerun the previously-used computational model of the supercritical NAPL dissolution system in the trapezoidal domain by setting the applied initial perturbation to be zero. Figure 10.17 shows the related computational simulation results, from which it can be observed that due to the dynamic behaviour of the supercritical NAPL dissolution system, the fingering phenomenon indeed takes place in the trapezoidal domain. This

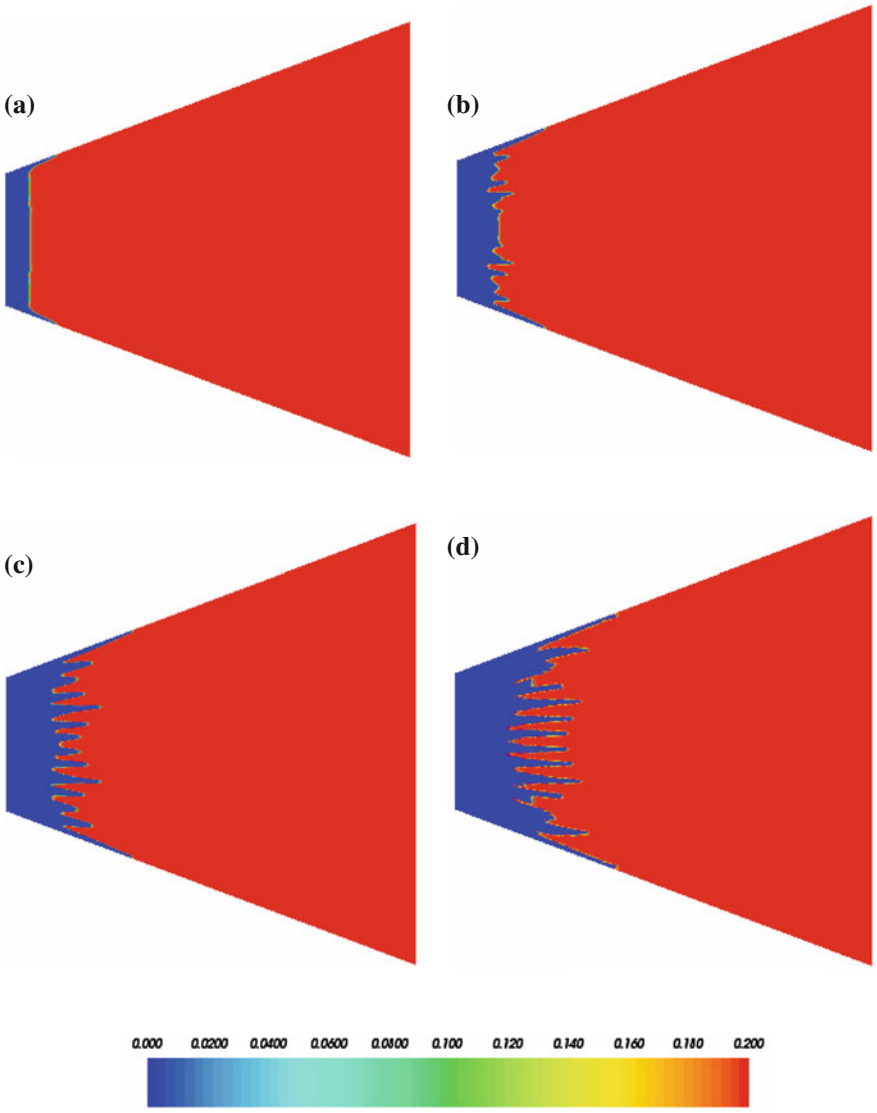

Fig. 10.17 The evolution of NAPL dissolution fronts in the trapezoidal domain consisting of fluid-saturated porous medium (Without applying initial perturbation): **a** $\theta = 20^\circ, \bar{t} = 160$; **b** $\theta = 20^\circ, \bar{t} = 320$; **c** $\theta = 20^\circ, \bar{t} = 640$; **d** $\theta = 20^\circ, \bar{t} = 1600$

indicates that the mesh discretization error, although it may be very small, can serve as a kind of small perturbation to trigger the fingering growth during the computational simulation of a supercritical NAPL dissolution system in the trapezoidal domain consisting of a fluid-saturated porous medium.

With two sets of computational simulation results of the supercritical NAPL dissolution system at hand, namely one obtained from the simulation with including an initial small perturbation and the other obtained from the simulation without including an initial small perturbation, it is possible to estimate the amplitude of the equivalent initial perturbation due to the discretization error in the supercritical NAPL dissolution system. As shown in Fig. 10.18, the ratio of the finger amplitude at $\bar{t} = 160$ to that at $\bar{t} = 128$ is equal to about 2.0 when the initial small perturbation, which has an amplitude of 0.002 (i.e. 0.01 S_{n0} as mentioned previously), is applied to the computational model of the NAPL dissolution system. This results in a dimensionless growth rate of 0.02166 (from Eq. (10.58)) for the NAPL dissolution system. On the other hand, the finger amplitude at $\bar{t} = 224$ when the initial small perturbation is not applied to the computational model is almost equal to that at $\bar{t} = 160$ when the initial small perturbation is applied to the computational model. From Eq. (10.59), this leads to a value of about 0.25 for R_2. Finally, substituting the value of R_2 into Eq. (10.60) yields a value of 0.00067 for the amplitude of the equivalent initial perturbation (i.e. δ_{A1}) due to the discretization error. Since δ_{A1} is smaller than 0.002 (i.e. $\delta_{A\text{initial}} = 0.002$), it is demonstrated that the effect of the total discretization error of the computational model is negligible in the computational simulations, compared with that of the initial small perturbation applied to the computational model. This also demonstrated that the proposed finger-amplitude growing theory associated with the mesh discretization error in the NAPL dissolution system of a trapezoidal domain in this study is useful for quantitatively assessing the correctness of computational simulations of NAPL dissolution-front instability problems in trapezoidal domains. If the amplitude of the equivalent initial perturbation due to the numerical discretization error is significantly smaller than the amplitude of the fingers generated by the numerical simulations of interest in the same geometry of the same finite element mesh, then one may safely neglect the numerical discretization effects on the numerical simulations of supercritical NAPL dissolution systems.

In summary, the propagation theory of the mesh discretization error associated with a NAPL dissolution system is first presented for a rectangular domain and then extended to a trapezoidal domain. This leads to the establishment of the finger-amplitude growing theory that is associated with both the corner effect and the mesh discretization effect in the NAPL dissolution systems of trapezoidal domains. This theory can be used to make the approximate error estimation of the corresponding computational simulation results. The related theoretical analysis and numerical results have demonstrated that: (1) both the corner effect and the mesh discretization effect can be quantitatively viewed as a kind of small perturbation so that they can have some considerable effects on the computational results of supercritical NAPL dissolution systems; (2) the proposed finger-amplitude growing theory associated with the corner effect at the entrance of a trapezoidal domain is useful for correctly explaining why the finger at either the top or the bottom boundary grows much faster than that within the interior of the trapezoidal domain; (3) the proposed finger-amplitude growing theory associated with the mesh discretization error in the NAPL dissolution system of a trapezoidal

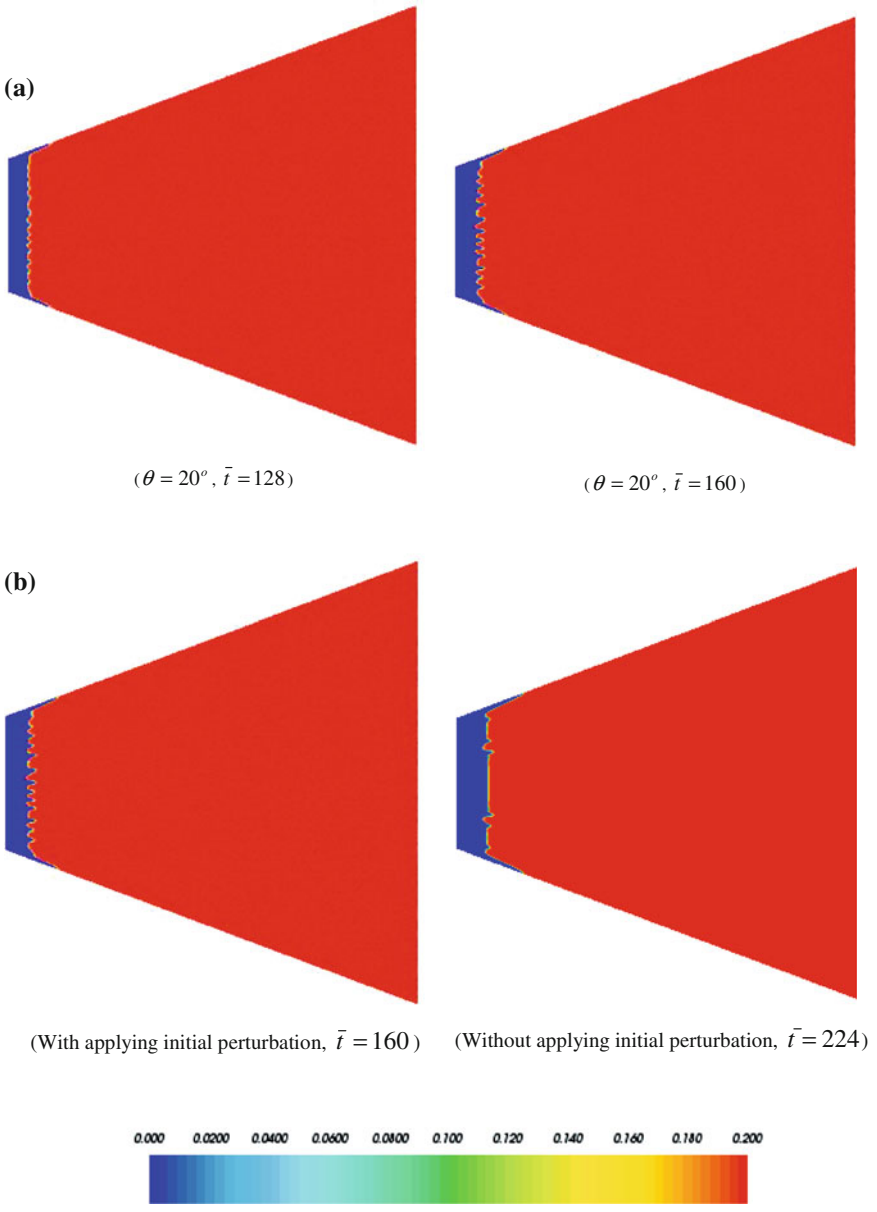

Fig. 10.18 Determination of the growth rate and equivalent initial perturbation in the supercritical NAPL dissolution system: **a** Determination of the growth rate; **b** Determination of the equivalent initial perturbation amplitude

domain can be used for quantitatively assessing the correctness of computational simulations of NAPL dissolution-front instability problems in trapezoidal domains, so that we can ensure that the computational simulation results are controlled by the physics of the NAPL dissolution system, rather than by the numerical artifacts.

References

Alt-Epping P, Smith L (2001) Computing geochemical mass transfer and water/rock ratios in submarine hydrothermal systems: implications for estimating the vigour of convection. Geofluids 1:163–181

Bear J (1972) Dynamics of fluids in porous media. American Elsevier Publishing Company, New York

Chadam J, Hoff D, Merino E, Ortoleva P, Sen A (1986) Reactive infiltration instabilities. IMA J Appl Math 36:207–221

Chadam J, Ortoleva P, Sen A (1988) A weekly nonlinear stability analysis of the reactive infiltration interface. IMA J Appl Math 48:1362–1378

Chen X, Jawitz JW (2008) Reactive tracer tests to predict nonaqueous phase liquid dissolution dynamics in laboratory flow chambers. Environ Sci Technol 42:5285–5291

Chen JS, Liu CW (2002) Numerical simulation of the evolution of aquifer porosity and species concentrations during reactive transport. Comput Geosci 28:485–499

Chen JS, Liu CW (2004) Interaction of reactive fronts during transport in a homogeneous porous medium with initial small non-uniformity. J Contam Hydrol 72:47–66

Chen JS, Liu CW, Lai GX, Ni CF (2009) Effects of mechanical dispersion on the morphological evolution of a chemical dissolution front in a fluid-saturated porous medium. J Hydrol 373:96–102

Christ JA, Ramsburg CA, Pennell KD, Abriola LM (2006) Estimating mass discharge from dense nonaqueous phase liquid source zones using upscaled mass transfer coefficients: an evaluation using multiphase numerical simulations. Water Resour Res 42:W11420. doi:10.1029/2006WR004886

Christ JA, Lemke LD, Abriola LM (2009) The influence of dimensionality on simulations of mass recovery from nonuniform dense non-aqueous phase liquid (DNAPL) source zones. Adv Water Resour 32:401–412

Daus AD, Frid EO, Sudicky EA (1985) Comparative error analysis in finite element formulations of the advection-dispersion equation. Adv Water Resour 8:86–95

DiFilippo EL, Carroll KC, Brusseau ML (2010) Impact of organic-liquid distribution and flow field heterogeneity on reduction in mass flux. J Contam Hydrol 115:14–25

Geller JT, Hunt JR (1993) Mass transfer from nonaqueous phase organic liquids in water-saturated porous media. Water Resour Res 29:833–845

Gerhard JI, Pang T, Kueper BH (2007) Time scales of DNAPL migration in sandy aquifers examined via numerical simulation. Ground Water 45:147–157

Grant GP, Gerhard JI (2007) Simulating the dissolution of a complex dense nonaqueous phase liquid zone: 1. Model to predict interfacial area. Water Resour Res 43:W12410. doi:10.1029/2007WR006038

Holzbecher EO (1998) Modeling density-driven flow in porous media. Springer, Berlin

Hong J, Hecker WC, Fletcher TH (1999) Predicting effectiveness factor for m-th order and langmuir rate equations in spherical coordinates. ACS Div Fuel Chem 44:1011–1015

Imhoff PT, Miller CT (1996) Dissolution fingering during the solubilization of nonaqueous phase liquids in saturated porous media: 1 Model predictions. Water Resour Res 32:1919–1928

Imhoff PT, Jaffe PR, Pinder GF (1994) An experimental study of complete dissolution of a nonaqueous phase liquid in saturated porous media. Water Resour Res 30:307–320
Imhoff PT, Thyrum GP, Miller CT (1996) Dissolution fingering during the solubilization of nonaqueous phase liquids in saturated porous media: 2 Experimental observations. Water Resour Res 32:1929–1942
Imhoff PT, Farthing MW, Gleyzer SN, Miller CT (2002) Evolving interface between clean and nonaqueous phase liquid (NAPL)-contaminated regions in two-dimensional porous media. Water Resour Res 38:1093–1106
Imhoff PT, Farthing MW, Miller CT (2003a) Modeling NAPL dissolution fingering with upscaled mass transfer rate coefficients. Adv Water Resour 26:1097–1111
Imhoff PT, Mann AS, Mercer M, Fitzpatrick M (2003b) Scaling DNAPL migration from the laboratory to the field. J Contam Hydrol 64:73–92
Kalia N, Balakotaiah V (2009) Effect of medium heterogeneities on reactive dissolution of carbonates. Chem Eng Sci 64:376–390
Maji R, Sudicky EA (2008) Influence of mass transfer characteristics for DNAPL source depletion and contaminant flux in a highly characterized glaciofluvial aquifer. J Contam Hydrol 102:105–119
Miller CT, Poirier-McNeil MM, Mayer AS (1990) Dissolution of trapped nonaqueous phase liquids: mass transfer characteristics. Water Resour Res 26:2783–2796
Miller CT, Christakos TG, Imhoff PT, McBride JF, Pedit JA, Trangenstein JA (1998) Multiphase flow and transport modeling in heterogeneous porous media: challenges and approaches. Adv Water Resour 21:77–120
Morris MI, Ball RC (1990) Renormalization of miscible flow functions. J Phys A: Math Gen 23:4199–4209
Ormond A, Ortoleva P (2000) Numerical modeling of reaction-induced cavities in a porous rock. J Geophys Res 105:16737–16747
Ortoleva P, Chadam J, Merino E, Sen A (1987) Geochemical self-organization II: The reactive-infiltration instability. Am J Sci 287:1008–1040
Parker JC, Park E (2004) Modeling field-scale dense nonaqueous phase liquid dissolution kinetics in heterogeneous aquifers. Water Resour Res 40:W05109. doi:10.1029/2003WR002807
Powers SE, Abriola LM, Weber WJ Jr (1994) An experimental investigation of nonaqueous phase liquid dissolution in saturated subsurface systems: transient mass transfer rates. Water Resour Res 30:321–332
Raffensperger JP, Garven G (1995) The formation of unconformity-type uranium ore deposits: coupled hydrochemical modelling. Am J Sci 295:639–696
Renard F, Gratier JP, Ortoleva P, Brosse E, Bazin B (1998) Self-organization during reactive fluid flow in a porous medium. Geophys Res Lett 25:385–388
Scheidegger AE (1961) General theory of dispersion in porous media. J Geophys Res 66:3273–3278
Seyedabbasi MA, Farthing MW, Imhoff PT, Miller CT (2008) The influence of wettability on NAPL dissolution fingering. Adv Water Resour 31:1687–1696
Soerens TS, Sabatini DA, Harwell JH (1998) Effects of flow bypassing and nonuniform NAPL distribution on the mass transfer characteristics of NAPL dissolution. Water Resour Res 34:1657–1673
Steefel CI, Lasaga AC (1990) Evolution of dissolution patterns: permeability change due to coupled flow and reaction. In: Melchior DC, Basset RL (eds) Chemical modeling in aqueous systems II, American Chemistry Society Symposium Series, vol 416, pp 213–225
Steefel CI, Lasaga AC (1994) A coupled model for transport of multiple chemical species and kinetic precipitation/dissolution reactions with application to reactive flow in single phase hydrothermal systems. Am J Sci 294:529–592
Tan CT, Homsy GM (1987) Stability of miscible displacements in porous media: radial source flow. Phys Fluids 30(5):1239–1245
Willson CS, Hall JL, Miller CT, Imhoff PT (1999) Factors affecting bank formation during surfactant-enhanced mobilization of residual NAPL. Environ Sci Technol 33:2440–2446

Yang Z, Yortsos YC (1998) Effect of no-flow boundaries on viscous fingering in porous media of large aspect ratio. Soc Petrol Eng J 3:285–292

Yeh GT, Tripathi VS (1991) A model for simulating transport of reactive multispecies components: model development and demonstration. Water Resour Res 27:3075–3094

Zhang C, Werth CJ, Webb AG (2007) Characterization of NAPL source zone architecture and dissolution kinetics in heterogeneous porous media using magnetic resonance imaging. Environ Sci Technol 41:3672–3678

Zhao C, Steven GP (1996a) A posteriori error estimator/corrector for natural frequencies of thin plate vibration problems. Comput Struct 59:949–963

Zhao C, Steven GP (1996b) An asymptotic formula for correcting finite element predicted natural frequencies of membrane vibration problems. Commun Numer Methods Eng 11:63–73

Zhao C, Steven GP (1996c) A practical error estimator for predicted natural frequencies of two-dimensional elastodynamic problems. Eng Comput 13:19–37

Zhao C, Hobbs BE, Hornby P, Ord A, Peng S, Liu L (2008a) Theoretical and numerical analyses of chemical-dissolution front instability in fluid-saturated porous rocks. Int J Numer Anal Meth Geomech 32:1107–1130

Zhao C, Hobbs BE, Ord A, Hornby P, Peng S (2008b) Effect of reactive surface areas associated with different particle shapes on chemical-dissolution front instability in fluid-saturated porous rocks. Transp Porous Media 73:75–94

Zhao C, Hobbs BE, Ord A, Hornby P, Peng S (2008c) Morphological evolution of three-dimensional chemical dissolution front in fluid-saturated porous media: a numerical simulation approach. Geofluids 8:113–127

Zhao C, Hobbs BE, Ord A (2009) Fundamentals of computational geoscience: numerical methods and algorithms. Springer, Berlin

Zhao C, Hobbs BE, Ord A, Peng S (2010a) Effects of mineral dissolution ratios on chemical-dissolution front instability in fluid-saturated porous media. Transp Porous Media 82:317–335

Zhao C, Hobbs BE, Ord A (2010b) Theoretical analyses of the effects of solute dispersion on chemical-dissolution front instability in fluid-saturated porous rocks. Transp Porous Media 84:629–653

Zhao C, Hobbs BE, Ord A (2010c) Theoretical analyses of nonaqueous-phase-liquid dissolution induced instability in two-dimensional fluid-saturated porous media. Int J Numer Anal Meth Geomech 34:1767–1796

Zhao C, Hobbs BE, Regenauer-Lieb K, Ord A (2011) Computational simulation for the morphological evolution of nonaqueous-phase-liquid dissolution fronts in two-dimensional fluid-saturated porous media. Comput Geosci 15:167–183

Zhao C, Hobbs BE, Ord A (2012) Effects of domain shapes on the morphological evolution of nonaqueous-phase-liquid dissolution fronts in fluid-saturated porous media. J Contam Hydrol 138–139:123–140

Zienkiewicz OC (1977) The finite element method. McGraw-Hill, London